Three-dimensional Mixed-Mode Linear Elastic Fracture Mechanics Analysis Using Domain Interaction Integrals

by

Ekrem Alp Esmen

Bachelor of Science in Mechanical Engineering,
Bachelor of Science in Economics,
University of Michigan at Ann Arbor, MI (2000)

Submitted to the Department of Mechanical Engineering
in partial fulfillment of the requirements for the degree of

Master of Science in Mechanical Engineering

at the

MASSACHUSETTS INSTITUTE OF TECHNOLOGY

June 2004

Author .....
Department of Mechanical Engineering
May 27, 2004

Certified by .....
David M. Parks
Professor of Mechanical Engineering
Thesis Supervisor

Accepted by .....
Ain A. Sonin
Chairman, Department Committee on Graduate Students

Three-dimensional Mixed-Mode Linear Elastic Fracture Mechanics Analysis Using Domain Interaction Integrals

by

Ekrem Alp Esmen

Submitted to the Department of Mechanical Engineering
on May 25, 2004, in partial fulfillment of the
requirements for the degree of
Master of Science in Mechanical Engineering

Abstract

Three-dimensional mixed-mode linear elastic fracture mechanics analysis is presented using domain interaction integrals. An out-of-plane sinusoidal crack was analyzed using a commercially available finite element package to extract the stress intensity factors and the J-Integral. The results were then compared with those obtained from crack face relative displacements as a post-processing step. The model has been tested on various geometries and the performance of focused and non-focused meshing algorithms are compared. The behavior of the stress intensity factors under far-field K-load for growing surface roughness in the form of a sinusoidal crack have been modelled as a cosine series.

Thesis Supervisor: David M. Parks
Title: Professor of Mechanical Engineering

Acknowledgments

I wish to express my deepest gratitude to my advisor Prof. David Parks for his constant encouragement, support and for teaching me the pleasure of doing research. I enjoyed working with him and learning from him.

Thanks to Ted, Steve, Vaibhaw, Nuo, Jin, Yin, Rajdeep, Nici, Adam, Mats, and Ray for their support and on-demand help.

My friends Jülide, Andrew, Hector, Alp, Göksel, and Onur made me feel home. My roommates Murat and Gökhan were always of great support though neither one of them could ever cook anything decent.

I am indebted to my family for their continuous support and motivation all through my life.

Contents

List of Figures

List of Tables

Chapter 1

Introduction

In 1983, the National Bureau of Standards released a study estimating the direct and indirect costs of fracture in the economy of the United States [1]. The study approximated the total annual loss at $ 120 billion - an amount equal to 4% of the gross national product at the time. Moreover, the study concluded that about one third of this loss could be avoided by implementing better fracture control.

Brittle fracture is characterized by very little plastic flow prior to failure and occurs as a result of a single crack propagating through the specimen. Griffith [2] introduced the energy approach to study crack propagation in glass specimens. His theory states that crack propagation occurs when the energy available for crack growth is sufficient to overcome the resistance of the material. Griffith proposed that there is a simple energy balance consisting of the decrease in the potential energy within the stressed body due to crack extension, balanced by the increase in surface energy due to increased crack surface area:

$$\frac{d\mathcal{W}}{d\mathcal{A}} - \frac{d\mathcal{U}}{d\mathcal{A}} = \gamma_s \tag{1.1}$$

where $\mathcal{W}$ is the external work done on the body, $\mathcal{U}$ is its internal strain energy, γ_s is the surface energy of the material, and $\mathcal{A} = 4at$ is the crack surface area for an internal crack in a body of thickness t (Figure 1-1). Griffith showed that the fracture stress in a through thickness crack in an infinitely wide plate subjected to a remote

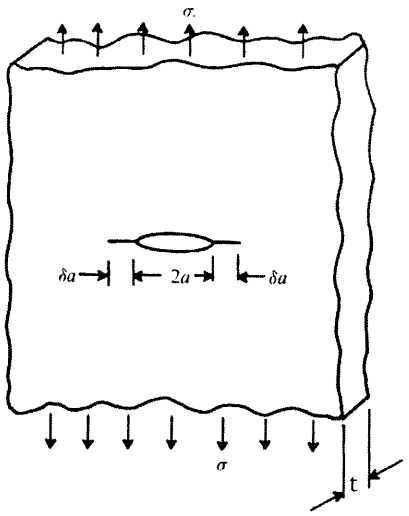

Figure 1-1: A large plate of an elastic material containing a crack length $2a$.

tensile stress σ is related to the crack size and can be given as:

$$\sigma_f = \sqrt{\frac{2E\gamma_s}{\pi a}} \tag{1.2}$$

where $2a$ is the length of the crack, γ_s is the surface energy of the material, and E is Young's Modulus. Griffith assumed that the energy consumed in crack propagation came exclusively from the surface energy of the material, neglecting the work required in producing a new plastic zone at the tip of the advancing crack. Hence, his approach only applies to ideally brittle solids. Irwin [3] extended Griffith's theory to metals to account for the limited plastic behavior near the crack-tip. The modified Griffith theory that includes the plastic dissipation, γ_p, can be expressed as

$$\sigma_f = \sqrt{\frac{2E(\gamma_s + \gamma_p)}{\pi a}} \tag{1.3}$$

where γ_p denotes the plastic energy per unit of crack extension at the crack-tip. The strain energy release rate in Equation 1.1 is denoted by $\mathcal{G}$ to give

$$\mathcal{G} = -\frac{d\Pi}{d\mathcal{A}} = \frac{d\mathcal{W}}{d\mathcal{A}} - \frac{d\mathcal{U}}{d\mathcal{A}} \tag{1.4}$$

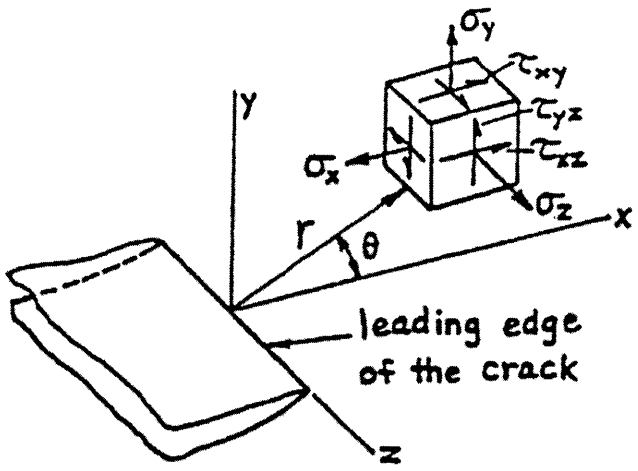

Figure 1-2: Stress field at the tip of a crack.

where Π is the potential energy of an elastic body. The Griffith-Irwin model applies to materials that exhibit small-scale yielding, and is therefore referred to as Linear Elastic Fracture Mechanics. Based on the cracked body solutions of Westergaard [4], Irwin [5] then provided a quantitative relation between the energy release rate (a global parameter) and the stress intensity factors (a local crack-tip parameter) for linear elastic isotropic bodies. The stress intensity factors, K_α, define the amplitude of the crack tip singularity. Moreover, the stress intensity factors completely define the crack tip conditions. Using the stress intensity factors, it is possible to solve - asymptotically - for all components of stress, strain, and displacement as a function of distance from the crack-tip. Placing the origin at the crack tip, the stress fields in a linear elastic cracked body can be given by

$$\sigma_{ij} = \frac{1}{\sqrt{2\pi r}} \left[K_I f_{ij}^I(\theta) + K_{II} f_{ij}^{II}(\theta) + K_{III} f_{ij}^{III}(\theta) \right] + \mathcal{O}(r^{1/2}) \tag{1.5}$$

where σ_{ij} is the stress tensor, r and θ represent the cylindrical coordinates (Figure 1-2), $f_{ij}(\alpha)$ are dimensionless functions of θ, and K_I, K_{II}, and K_{III} are the stress intensity factors corresponding to the three basic modes of loading. Though the higher-order terms depend on the geometry, the solution for any given configuration

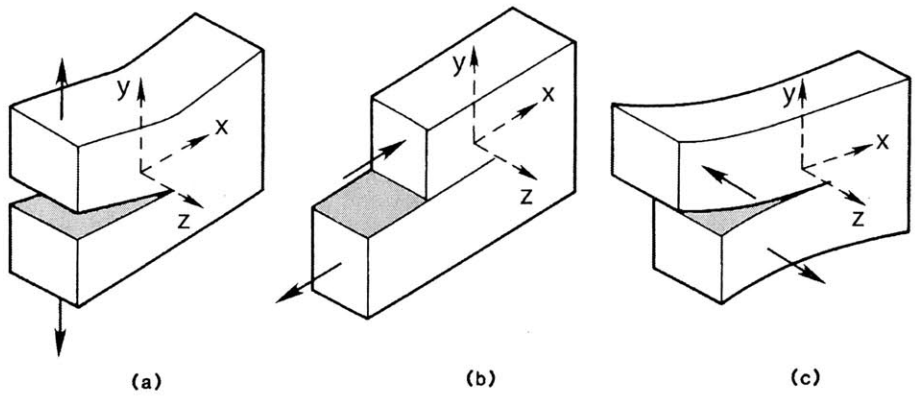

Figure 1-3: The three modes of cracking (a) opening mode (mode I) (b) sliding mode (mode II) (c) tearing mode (mode III).

contains a leading term that is proportional to $1/\sqrt{r}$. Therefore, in the vicinity of the crack-tip the higher-order terms can be neglected where the stress singularity at the crack-tip is implied.

A crack in a model can be stressed in three modes (Figure 1-3). In mode I, the principal load is applied normal to the crack plane. The displacements of the crack faces are perpendicular to the plane of the crack. Mode II is in-plane shear, and the displacement of the crack faces is in the plane of the crack and perpendicular to the leading edge of the crack. Mode III is out-of-plane shear, and the crack face displacements are in the plane of the crack and parallel to the leading edge of the crack. The stress state ahead of the crack tip then reduces to

$$\lim_{r\to 0} \sigma_{ij}^{(\alpha)} = \frac{K_{(\alpha)}}{\sqrt{2\pi r}} f_{ij}^{(\alpha)}(\theta), \quad (no\ sum\ on\ \alpha = I, II, III). \tag{1.6}$$

Irwin [5] proved that the energy release rate $\mathcal{G}$ is uniquely related to the stress intensity factor K for isotropic linear elastic materials. By calculating the change in potential energy as the crack propagates by a distance δa, Irwin was able to show:

$$\mathcal{G} = \frac{1}{E'}(K_I^2 + K_{II}^2) + \frac{1}{2G}K_{III}^2 \tag{1.7}$$

where the material properties are given as

$$E = 2(1+\nu)G$$

and

$$E' = E/(1-\nu^2)$$

for plane strain. In Chapter 2, we will show the equivalence of J and the energy release rate $\mathcal{G}$, and express J in terms of the stress intensity factors as

$$J = \frac{1}{E'}(K_I^2 + K_{II}^2) + \frac{1}{2G}K_{III}^2. \tag{1.8}$$

If a brittle isotropic solid were ideally elastic, we would expect the solution in Equation 1.5 to become more accurate as we approach the crack-tip. Moreover, as we move farther away from the crack-tip, the asymptotic crack-tip field would not be accurate as the fields are influenced by the geometry of the solid and boundary conditions in a finite-sized body. However, our linear elastic model predicts infinite stress at the crack tip, which no material could withstand. Therefore, we predict our solution is not accurate very close to the crack tip either. Hence, we can divide the material into three regions: plastic zone near the crack tip, a region further away from the crack tip where the LEFM is expected to be accurate, and the far field, where the stress fields depend on the geometry of the solid and boundary conditions. The region where the LEFM is expected to give accurate results is known as the "K-dominant" zone. The fields in this region are assumed to depend only on K_I, K_{II} and K_{III}.

A cracked body can be loaded in any of these three modes, or a combination of two or three modes. Even though most of the practical problems are of the mixed-mode type, the bulk of the fracture mechanics work has been concentrated on the "opening mode" or Mode I crack growth problems. This is justified by the simplicity of its application and by its dominant effect on the crack growth in a component. A mixed-mode $K_I - K_{II}$ problem can be modelled in two dimensions in a crack oriented at an acute angle to the applied stress, or more generally when the applied stress is biaxial. A mixed-mode analysis combining all three fracture modes can be modelled in three dimensions.

In the following chapters, two further sets of elastic crack parameters are introduced: the J-Integral and the Crack Face Relative Displacement (CFRD). They are used in the remainder of this work and so are developed in some detail from background information.

J-Integral evaluation based on the virtual crack extension/domain integral method has proven useful to evaluate the variation of fracture mechanics singularities strength along a 3-D crack-front. Moran and Shih [6, 7] presented a discussion of the domain integral method, where a crack-tip contour integral is expressed as a volume integral over a finite domain surrounding the crack-tip. The interaction energy integral method is an implementation of the domain integral method where auxiliary fields are introduced and superimposed on top of the actual fields that come from the solution to the problem. The auxiliary fields can be related to the mixed-mode stress intensity factors by defining the interaction integral as a crack-tip contour integral surrounding a point on the crack front, defined in the limit as the contour is shrunk on to the crack tip. Stern, Becker, and Dunham [8] introduced the interaction energy integral approach to compute mixed-mode stress intensity factors in two-dimensional crack problems. The process can be generalized for three-dimensional analysis. In an auxiliary field, the desired mode is set to a constant value (e.g. unity) while the remaining two modes are set to zero. The interaction with the real fields leaves only the terms involving the non-zero auxiliary field with one equation and three unknowns, namely the real K_I, K_{II}, and K_{III}. Repeating the same procedure for the other two auxiliary modes, we obtain three equations and three unknowns and solve for the desired stress intensity factors in the mixed-mode analysis.

The Crack Front Relative Displacement (CFRD) - or the crack tip opening displacement as it is called in two dimensional, pure mode I geometry - is another fracture parameter that is equivalent to the LEFM criteria when LEFM is applicable. For the purposes of this study, CFRD serves to verify the accuracy of the stress intensity factors obtained from other parameters.

Gosz and Moran [9] explored the concept of mixed-mode stress intensity factors along non-planar crack fronts in three dimensions. Gao and Rice [10] presented a

slightly curved crack front analysis for general shear loading of planar crack faces. However, there is still a need to explore the behavior of three-dimensional cracks with out-of-plane fronts where the geometry of a crack and its loading activates all three stress modes due to, e.g. a crack surface roughness. In Chapter 4, we analyze a finite-width plate of thickness t containing a through-thickness flat crack (Figure 4-1). The stress intensity factors are calculated through the interaction integrals. Moreover, the J-Integrals are calculated both from the stress intensity factors and directly through domain integration to verify the equivalency of the two methods. Next, the accuracy of the stress intensity factors are verified through the K's calculated from the CFRD method. The results are normalized by reference solutions and plotted on top of each other. Next, a mixed-mode problem is created by generating a surface roughness in the form of an out of plane sinusoidal crack across the thickness. Similarly, the stress intensity factors and J-Integral calculations are plotted against each other in this mixed-mode problem where all three modes are present. Discrepancies between the results obtained from different methods for the mixed-mode crack have been observed, and various boundary conditions are tested to further investigate the patterns of this behavior. Then loading is applied by a far-field K_I loading to extend the reach of the "K-dominant" zone, and to verify the extent of the curious behavior in the mixed-mode problem. Finally, a general pattern of stress intensity factors vs. sinusoidal surface roughness in the form of a cosine function of growing amplitude is established.

All the meshes used in this study were created using MATLAB. Moreover, extensive post-processing was performed. The Appendix contains the algorithms behind programming done in MATLAB. The included CD has a copy of selected ABAQUS input files used to run the simulations.

Chapter 2

J-Integral

The path-independent J-Integral introduced by Rice [11] is a fracture characterizing parameter for nonlinear materials. The J-Integral can also be interpreted as the energy release rate in elasticity. The potential energy of an elastic body in two dimensions in the absence of body forces can be given as

$$\Pi(a) = \int_{\mathcal{A}} W \, d\mathcal{A} - \int_{\Gamma'} T_i u_i ds$$

where Γ' is the portion of the boundary contour on which tractions are defined, and $\mathcal{A}$ is the total area of a two dimensional body (Figure 2-1). The crack surfaces are taken to be traction free, and the tractions are assumed to be independent of the crack length a. The change in potential energy resulting from a virtual crack extension of the crack is

$$\frac{d\Pi}{da} = \int_{\mathcal{A}} \frac{dW}{da} d\mathcal{A} - \int_{\Gamma'} T_i \frac{du_i}{da} d\gamma. \tag{2.1}$$

The coordinate system is attached to the crack tip; thus a derivative with respect to crack length can be written as

$$\frac{d}{da} = \frac{\partial}{\partial a} + \frac{\partial x}{\partial a}\frac{\partial}{\partial x} = \frac{\partial}{\partial a} - \frac{\partial}{\partial x}$$

since $\partial x/\partial a = -1$. Applying this result to Equation 2.1 gives

$$\frac{d\Pi}{da} = \int_{\mathcal{A}} \left(\frac{\partial W}{\partial a} - \frac{\partial W}{\partial x} \right) d\mathcal{A} - \int_{\Gamma'} T_i \left(\frac{\partial u_i}{\partial a} - \frac{\partial u_i}{\partial x} \right) d\gamma$$

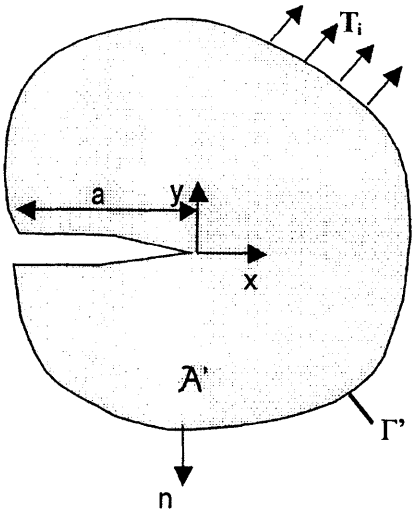

Figure 2-1: Free body diagram of a two-dimensional cracked body bounded by Γ'.

using definition of strain energy

$$\frac{\partial W}{\partial x} = \frac{\partial W}{\partial \varepsilon_{ij}} \frac{\partial \varepsilon_{ij}}{\partial x} = \sigma_{ij} \frac{\partial \varepsilon_{ij}}{\partial x}.$$

The strain-displacement relationship for small strain gives

$$\frac{\partial W}{\partial x} = \frac{1}{2} \sigma_{ij} \left[\frac{\partial}{\partial x} \left(\frac{\partial u_i}{\partial x_j} \right) + \frac{\partial}{\partial x} \left(\frac{\partial u_j}{\partial x_i} \right) \right] = \sigma_{ij} \frac{\partial}{\partial x_j} \left(\frac{\partial u_i}{\partial x} \right)$$

due to symmetry ($\sigma_{ij} = \sigma_{ji}$). Invoking the principle of virtual work gives

$$\int_{\mathcal{A}'} \frac{\partial W}{\partial a} d\mathcal{A} = \int_{\mathcal{A}'} \sigma_{ij} \frac{\partial}{\partial a} \left(\frac{\partial u_i}{\partial x} \right) d\mathcal{A} = \int_{\Gamma'} T_i \frac{\partial u_i}{\partial a} d\gamma.$$

Therefore, Equation (2.1) reduces to

$$\frac{d\Pi}{da} = -\int_{\mathcal{A}} \frac{\partial W}{\partial x} d\mathcal{A} + \int_{\Gamma'} T_i \frac{\partial u_i}{\partial x} d\gamma. \tag{2.2}$$

Applying the divergence theorem and multiplying both sides by -1 leads to

$$-\frac{d\Pi}{da} = \int_{\Gamma'} \left(W n_x - T_i \frac{\partial u_i}{\partial x} \right) d\gamma = \int_{\Gamma'} W dy - T_i \frac{\partial u_i}{\partial x} d\gamma$$

since $n_x d\gamma = dy$. Rice [11] considered a counterclockwise arbitrary contour Γ from the lower to the upper crack face around the crack tip (Figure 2-2(a)) where the

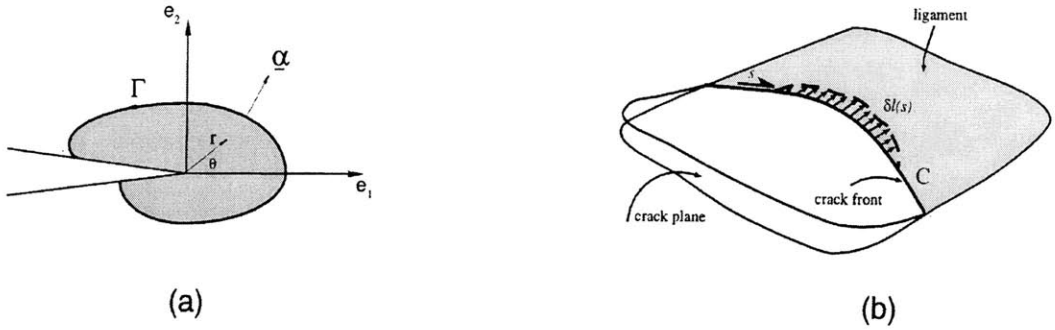

Figure 2-2: Definition of the J-Integral. (a) Contour for the evaluation of the J-Integral. (b) Crack-front perturbation field $\delta l(s)$.

traction can be written in terms of the Cauchy stress and the outward normal $\boldsymbol{\alpha}$ to Γ as $T_i = \sigma_{ij}\alpha_j$ to define J:

$$J = \int_\Gamma \left(W\alpha_1 - \sigma_{ij}\alpha_j \frac{\partial u_i}{\partial x_1} \right) d\gamma, \tag{2.3}$$

where W is the strain energy density defined by

$$W(\epsilon_{kl}) = \int_0^{\epsilon_{kl}} \sigma_{ij} d\epsilon_{ij}.$$

From Equation (2.2), the potential energy per unit thickness $\tilde{\pi}$ in plane strain can be given as

$$\tilde{\pi} = \int_{\mathcal{A}} W\left(\epsilon_{ij}\right) d\mathcal{A} - \int_{\partial \mathcal{A}_T} T_i\, u_i\, d\gamma, \tag{2.4}$$

where $\mathcal{A}_T$ is the portion of the boundary where the tractions are prescribed. The strain energy release rate $\mathcal{G}$ (Chapter 1) can be be then expressed as

$$\mathcal{G} = -\frac{\partial \tilde{\pi}}{\partial l}|_T$$

where the decrease in $\tilde{\pi}$ due to a unit advance of crack in its plane with tractions held fixed. Then, to the first order,

$$\mathcal{G}\,\delta l = -\,\delta\tilde{\pi}. \tag{2.5}$$

By introducing a point-wise definition of the energy release rate $\mathcal{G}$ as a function of the arc-length measuring curvilinear coordinate, s, along the crack front C, we can generalize expression (2.5) to three-dimensional problems [12, 13]. Let $\delta l(s)$ denote the magnitude of the virtual crack advance at s, in the plane of the crack and in the direction normal to the crack-front, as shown in Figure 2-2(b). Equation (2.5) can be recast, to within first-order terms in $\delta l(s)$, as

$$\int_C \mathcal{G}(s)\, \delta l(s)\, ds = -\delta\pi, \tag{2.6}$$

where ds is the elemental arc length along C, and $-\delta\pi$ is the decrease in the potential energy of the body.

For a plane strain tensile crack, with the crack advancing uniformly through the thickness in its plane [14], J and $\mathcal{G}$ are equivalent in two dimensions. Along a 3-D crack-front, as $r \rightarrow 0^+$, asymptotic plane strain conditions prevail so that the three-dimensional singular stress fields approach a linear combination of Mode III and the plane strain two-dimensional Mode I and Mode II fields along C. Hence, as Γ shrinks onto the crack front, $\Gamma \rightarrow \Gamma_0$, the local value of the energy release rate, $\mathcal{G}(s)$, and point-wise value of the J-integral, $J(s)$, become equivalent:

$$\mathcal{G}(s) = \lim_{\Gamma \rightarrow \Gamma_0} \int_{\Gamma(s)} [W\, \alpha_k\, n_k - \sigma_{ij}\, \alpha_j\, u_{i,k}\, n_k]\, d\gamma = J_{\Gamma_0}(s) = J(s), \tag{2.7}$$

where $\mathbf{n}$ is the in-plane normal to the crack-front at location s. Equation (2.6) can then be written as

$$\int_C J(s)\, \delta l(s)\, ds = -\delta\pi, \tag{2.8}$$

with the understanding that $J(s)$ is defined through (2.7).

2.1 Domain Integral Representation

The crack tip contour integrals are difficult to evaluate in numerical studies and may result in inaccurate readings. The difficulty lies in the nature of the calculations where

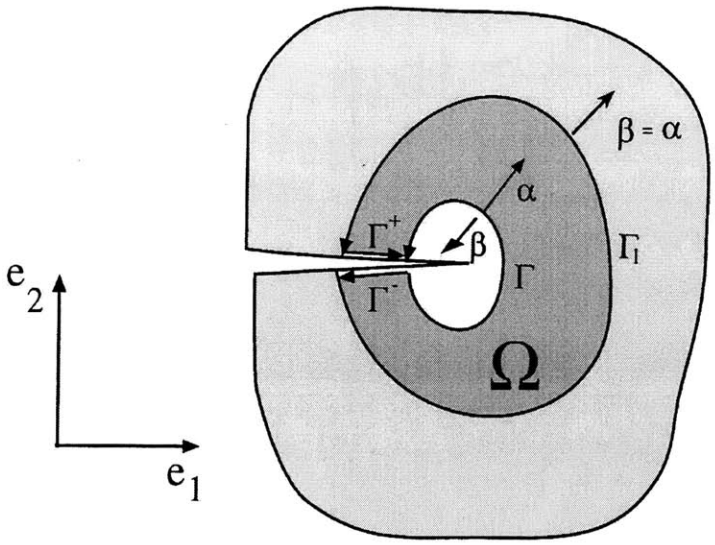

Figure 2-3: Two-dimensional formulation. Domain of integration Ω.

the crack tip energy release rate in these integrals need to be calculated at points arbitrarily close to the crack tip [7]. Yet, it is near the crack-tip where accurate solutions are most difficult to obtain. The domain integral method provides a convenient way to calculate the energy release rate for 2-D and 3-D problems [14]. The finite element formulation of the domain integral method corresponds to the virtual crack extension method [15], which is versatile in its applicability to 3-D crack configurations. Both formulations have been derived in greater detail in [12].

2.1.1 Two-dimensional formulation

Introducing Eshelby's energy momentum tensor [16], $P_{1j} = W\,\delta_{1j} - \sigma_{ij}\,u_{i,1}$, we can recast (2.3) in the more compact form

$$J = \int_{\Gamma} [W\,\delta_{1j} - \sigma_{ij}\,u_{i,1}]\;\alpha_j\,d\gamma = \int_{\Gamma} P_{1j}\,\alpha_j\,d\gamma. \tag{2.9}$$

We now consider a second curve around the crack tip, Γ_1, surrounding an arbitrary interior boundary Γ, and define a simply-connected region, Ω, between Γ_1 and Γ,

as shown in Figure 2-3. Ω is bounded by closed curve $\Psi = \Gamma_1 + \Gamma^+ - \Gamma + \Gamma^-$. The path-independence of J [11] gives

$$J = \int_{\Gamma} P_{1j}\, \alpha_j \, d\gamma = \int_{\Gamma_1} P_{1j}\, \alpha_j \, d\gamma. \tag{2.10}$$

We define a vector $\boldsymbol{\beta}$ as the outward normal to Ψ, such that $\boldsymbol{\beta} = -\boldsymbol{\alpha}$ on Γ, and $\boldsymbol{\beta} = \boldsymbol{\alpha}$ on Γ_1. If the crack faces are traction-free, then $\sigma_{ij} \cdot \beta_j = 0_i$ on Γ^+ and Γ^-. Also on Γ^+ and Γ^- the vector $\boldsymbol{\beta}$ is normal to the direction of crack propagation, $\beta_1 = 0$, so that (2.5) can be written as

$$-\delta\tilde{\pi} = \mathcal{G}\, \delta l = J\, \delta l = \int_{\Psi} \left[W\, \delta_{1j} - \sigma_{ij}\, u_{i,1} \right] q_1 \beta_j \, d\gamma = \int_{\Psi} P_{1j}\, q_1\, \beta_j \, d\gamma, \tag{2.11}$$

where we introduce a sufficiently smooth C^0 vector-valued perturbation field $\mathbf{q} = q_1 \mathbf{e}_1$ defined in Ω which has magnitude δl on Γ and which vanishes on Γ_1:

$$q_1 \equiv \begin{cases} \delta l & \text{on and within } \Gamma, \\ 0 & \text{on } \Gamma_1. \end{cases}$$

Application of the divergence theorem reduces (2.11) to

$$-\delta\tilde{\pi} = J\, \delta l = \int_{\Omega} (P_{1j}\, q_1)_{,j} \, dA = \int_{\Omega} (P_{1j,j}\, q_1 + P_{1j}\, q_{1,j}) \, dA. \tag{2.12}$$

2.1.2 Three-dimensional formulation

For three-dimensional crack configurations, (2.7) and (2.8) can be combined to express the decrease in total potential energy as

$$-\delta\pi = \int_C \delta l(s) \left[\lim_{\Gamma \to \Gamma_0} \int_{\Gamma} P_{mj}\, n_m\, \alpha_j \, d\gamma \right] ds, \tag{2.13}$$

where the momentum tensor $\mathbf{P}$ is defined as $P_{mj} = \frac{1}{2}\, \sigma_{ik} \varepsilon_{ik} \delta_{mj} - \sigma_{ij} u_{i,m}$.

Introducing surface S_0 as the envelope of the curves $\Gamma_0(s)$ as shown in Figure 2-4 (a), we can write (2.13) as

$$-\delta\pi = \lim_{S \to S_0} \int_S P_{mj}\, n_m\, \alpha_j\, \delta l(s) \, dS. \tag{2.14}$$

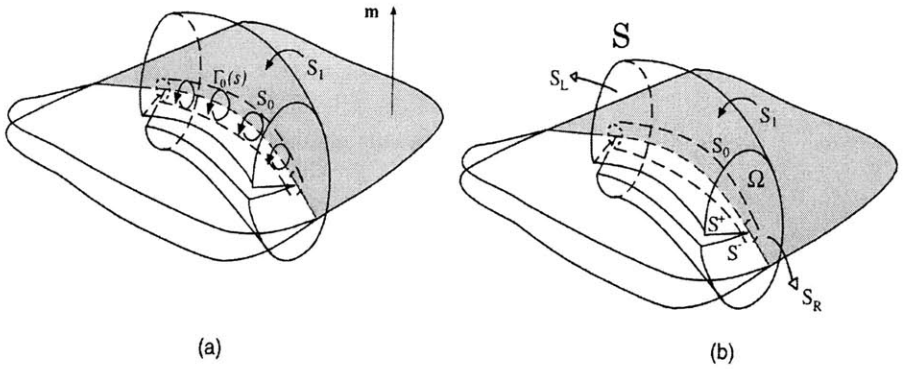

Figure 2-4: Three-dimensional formulation. (a) Surfaces S_0 and S_1 enclosing the crack-front. (b) 3D domain of integration, Ω in the limit $\Gamma_0 \to 0$.

Now consider a second cylindrical surface around the crack tip, S_1, exterior to S_0, and define a three-dimensional simply-connected domain Ω between S_0 and S_1, as shown in Figure 2-4 (b). Ω is bounded by the closed surface $\mathcal{S}$ formed by the surfaces $S_0, S_1, S^+, S^-, S_R, S_L$, where S^+ and S^- are surfaces on the respective crack faces, and S_R and S_L connect S_0 and S_1 at the respective ends of the cylindrical domain as shown in Figure 2-4 (b). We define a vector $\boldsymbol{\beta}$ as the outward normal to $\mathcal{S}$, such that $\boldsymbol{\beta} = -\boldsymbol{\alpha}$ on S_0; also the traction-free crack surfaces S^- and S^+ have their respective outward normals $\boldsymbol{\beta} = \pm\mathbf{m}$, where $\mathbf{m}$ is the normal to crack plane. We consider a sufficiently smooth C° virtual crack advance pattern, $\delta l(s)$, which vanishes at all crack locations outside the Ω-domain, and the corresponding perturbation field, $\mathbf{q}$, in Ω as

$$\mathbf{q} \equiv \begin{cases} \delta l(s)\,\mathbf{n}(s) & \text{on the crack front,} \\ \mathbf{0} & \text{on } S_1, \\ \mathbf{0} & \text{on } S_R \cup S_L, \\ \mathbf{q}\cdot\mathbf{m} = \mathbf{0} & \text{on } S^+ \cup S^-. \end{cases}$$

The third condition applies only if S_L and S_R are not free external surfaces of the body. If an end surface is a free surface with normal $\mathbf{m}$, then $\mathbf{q}\cdot\mathbf{m} = \mathbf{0}$. If the crack faces are traction free, $\sigma_{ij}\beta_j = 0_i$ on S^+ and S^-, so that $q_m P_{mj}\beta_j = 0$ on S^+ and S^-.

Combining these results with (2.14), we obtain

$$-\delta\pi = \int_S [P_{mj}\, q_m\, \beta_j]\, dS. \tag{2.15}$$

Application of the divergence theorem to (2.15) leads to

$$-\delta\pi = \int_\Omega [(W\delta_{mj} - \sigma_{ij}\, u_{i,m})\, q_{m,j} + (W\delta_{mj} - \sigma_{ij}\, u_{i,m})_{,j}\; q_m]\, dV. \tag{2.16}$$

2.2 Interaction Energy Integral Method

The energy release rate can be given as [17]

$$I = \frac{1}{8\pi}\mathbf{K}^T\mathbf{B}^{-1}\mathbf{K}, \tag{2.17}$$

where $\mathbf{K} = [K_I, K_{II}, K_{III}]^T$. For isotropic materials, $\mathbf{B}$ is diagonal with the components

$$B_{11} = B_{22} = \frac{\mu}{4\pi(1-\nu)} \text{ and } B_{33} = \frac{\mu}{4\pi}, \tag{2.18}$$

and the expression can be restated as

$$I = \frac{1-\nu}{2\mu}[K_I^2 + K_{II}^2] + \frac{1}{2\mu}K_{III}^2. \tag{2.19}$$

Note that, for actual, mixed-mode crack field, the crack extension force is given by

$$I = \frac{1}{8\pi}\,[K_I B_{11}^{-1} K_I + (\textit{terms not involving } K_I)]. \tag{2.20}$$

An auxiliary field can be defined as explained in Stern, Becker, and Dunham [8] or in Gosz and Moran [9]. In most cases, the auxiliary stress fields are assumed divergence free and set to zero. However, Gosz and Moran [9] note that is not necessarily the case in three-dimensions and the divergence of the auxiliary stress field is not necessarily zero. In a three-dimensional geometry, spatially varying components $\sigma_{ij}^{(aux)}$ and basis vectors $\hat{\mathbf{e}}_i$ of the auxiliary stress tensor $\boldsymbol{\sigma}^{(aux)}$ can lead to divergence. The

energy release rate for any such pure mode I field with stress intensity factor $K_I^{(aux)}$ where $K_{II}^{(aux)} = K_{III}^{(aux)} = 0$ can be formulated as

$$I_{(aux)}^{I} = \frac{1}{8\pi} K_I^{(aux)} B_{11}^{-1} K_I^{(aux)}. \tag{2.21}$$

Superimposing the auxiliary field onto the actual field yields

$$\begin{aligned} I_{tot} &= \frac{1}{8\pi} [(K_I + K_I^{(aux)}) B_{11}^{-1} (K_I + K_I^{(aux)}) \\ &\quad + (\textit{terms not involving } K_I \textit{ or } K_I^{(aux)})]. \end{aligned} \tag{2.22}$$

Since the terms not involving K_I or $K_I^{(aux)}$ in I_{tot}^{I} and I are equal, the interaction integral for isotropic materials can be defined as

$$\begin{aligned} I_{int} &= I_{tot} - I - I_{(aux)} \\ &= \frac{1}{8\pi} (2K_I^{(aux)} B_{11}^{-1} K_I) \end{aligned} \tag{2.23}$$

I_{tot} is the energy release rate of the total field (the actual field plus the auxiliary field), and $I_{(aux)}$ is the energy release rate of the auxiliary field. The interaction energy integral in the line integral form, by letting $P_{1j}^{(int)} = \sigma_{ik}\varepsilon_{ik}^{(aux)}\delta_{1j} - u_{i,1}^{(aux)}\sigma_{ij} - u_{i,1}\sigma_{ij}^{(aux)}$, can be written as

$$I_{int} = \int_{\Gamma} (\sigma_{ik}\varepsilon_{ik}^{(aux)}\delta_{1j} - \sigma_{ij}u_{i,1}^{(aux)} - \sigma_{ij}^{(aux)}u_{i,1})\, \alpha_j \, d\gamma \tag{2.24}$$

assuming small strains in the absence of body forces. To convert this interaction energy contour integral into an equivalent area integral we employ the same methodology as in the J-Integral conversions, including the vector valued perturbation field $\mathbf{q}$ over the same domain (Figure 2-3). Then,

$$I_{int} = -\int_{\Omega} P_{1j}^{(int)} q_{1,j} d\mathcal{A} - \int_{\Omega} P_{1j,j}^{(int)} q_1 d\mathcal{A}.$$

Then, the interaction integral can be written as

$$I_{int} = \int_{\Omega} \left(\sigma_{ik}\varepsilon_{ik}^{(aux)}\delta_{1j} - \sigma_{ij}u_{i,1}^{(aux)} - \sigma_{ij}^{(aux)}u_{i,1}\right) q_{1,j} d\mathcal{A}$$

$$+\int_{\Omega}\left(\sigma_{ik,1}\varepsilon_{ik}^{(aux)}-\sigma_{ij,j}^{(aux)}u_{i,1}+\sigma_{ik}\varepsilon_{ik,1}^{(aux)}-\sigma_{ij}u_{i,1j}^{(aux)}-\sigma_{ij}^{(aux)}u_{i,1j}\right)q_1\,d\mathcal{A}. \tag{2.25}$$

where $\sigma_{ij,j}u_{i,1}^{(aux)}=0$ due to lack of body forces.

The three-dimensional formulation for the line integrals can be set in a similar way. In three dimensions, following the guidelines laid out in the domain representation of the J-Integral formulation, the three dimensional line integral formulation can be given as

$$I_{int}=\lim_{S\to S_0}\int_S P_{mj}^{(int)}n_m\alpha_j\delta l(s)dS, \tag{2.26}$$

where all parameters are defined as in the three dimensional J volume integral calculations. Application of divergence theorem gives

$$\begin{aligned}I_{int} &= \int_{\Omega}\left(\sigma_{ik}\varepsilon_{ik}^{(aux)}\delta_{mj}-\sigma_{ij}u_{i,m}^{(aux)}-\sigma_{ij}^{(aux)}u_{i,m}\right)q_{m,j}dV\\ &+\int_{\Omega}\left(\sigma_{ik,m}\varepsilon_{ik}^{(aux)}-\sigma_{ij,j}^{(aux)}u_{i,m}+\sigma_{ik}\varepsilon_{ik,m}^{(aux)}-\sigma_{ij}u_{i,mj}^{(aux)}-\sigma_{ij}^{(aux)}u_{i,mj}\right)q_m\,dV.\end{aligned} \tag{2.27}$$

All three energy release rates I,I_{tot}, and $I_{(aux)}$, including I_{int} itself can be computed from the domain integrals. Repeating the calculations for mode II and mode III, a linear system of equations results:

$$I_{int}^{\alpha}=\frac{1}{4\pi}K_{\alpha}^{(aux)}B_{\alpha\beta}^{-1}K_{\beta},\qquad\text{(no sum on }\alpha=\mathrm{I,II,III};\ \text{sum on }\beta). \tag{2.28}$$

If the K_{α}^{aux} are assigned unit values, the solution for $\mathbf{K}$'s leads to

$$\mathbf{K}=4\,\pi\,\mathbf{B}\,\mathbf{I}_{int} \tag{2.29}$$

where $\mathbf{I}_{int}=[I_{int}^{I},I_{int}^{II},I_{int}^{III}]^T$.

Chapter 3

Crack Face Relative Displacement (CFRD)

The Crack Face Relative Displacement method has been used in the analysis to verify the accuracy of results obtained by FEM solutions. The analytical solution for pure Mode I for the flat crack exists and served to verify the accuracy of the initial CFRD post-processing code, as well as the ABAQUS model. The CFRD method is crucial for determining the accuracy of the sinusoidal crack solution, as there are no analytical solutions for the mixed mode problems examined.

The node displacements used to calculate the stress intensity factors are captured from an ABAQUS report for the node set near the crack front, as explained in Appendix A. The postprocessing provided a value for each loading mode by making use of local coordinate systems along the crack and the equations derived below. These derivations are adopted from [18].

3.1 Asymptotic Crack Tip Fields

3.1.1 Antiplane Strain

Antiplane strain is defined as a state where $u_1 = u_2 = 0$ and $u_3 = u_3(X_1, X_2)$. The nonzero scalar components of strain have the form $\varepsilon_{\alpha 3} = \varepsilon_{\alpha 3}(X_1, X_2)$, where

$$\varepsilon_{\alpha 3} = \frac{1}{2} u_{3,\alpha}. \tag{3.1}$$

Therefore, the nontrivial scalar components of stress, $\sigma_{ij} = 2\mu\varepsilon_{ij} + \lambda\varepsilon_{kk}\delta_{ij}$, in the form $\sigma_{\alpha 3} = \sigma_{\alpha 3}(X_1, X_2)$, are given in

$$\sigma_{\alpha 3} = \mu u_{3,\alpha}. \tag{3.2}$$

In the absence of body forces the only relevant equation of equilibrium is

$$\sigma_{\alpha 3,\alpha} = 0. \tag{3.3}$$

Equations (3.1)–(3.3) can be combined to yield Laplace' s equation

$$\nabla^2 u_3 = u_{3,\alpha\alpha} = 0. \tag{3.4}$$

An antiplane strain displacement field u_3 can be presented as the real part of an analytic function ψ of the complex variable $z = X_1 + iX_2$,

$$u_3 = \frac{1}{\mu} \Re[\psi(z)]. \tag{3.5}$$

Then, it follows from the Cauchy-Riemann equations that $\nabla^2 u_3 = 0$ at points where $\psi(z)$ is analytic. It follows from (3.2) and (3.3) that, at points where $\psi(z)$ is analytic,

$$\sigma_{\alpha 3} = \frac{\partial}{\partial X_\alpha} \Re[\psi(z)] = \Re\left[\frac{\partial}{\partial X_\alpha} \psi(z)\right] = \Re\left[z_{,\alpha}\, \psi'(z)\right]$$

Since $z_{,1} = 1$ and $z_{,2} = i$,

$$\sigma_{13} = \Re[\psi'(z)], \ \sigma_{23} = \Re[i\psi'(z)] = -\Im[\psi'(z)]$$

or

$$\sigma_{13} - i\sigma_{23} = \psi'(z) \tag{3.6}$$

which gives the nonzero components of stress in terms of the antiplane strain complex potential, at points where the complex potential is analytic.

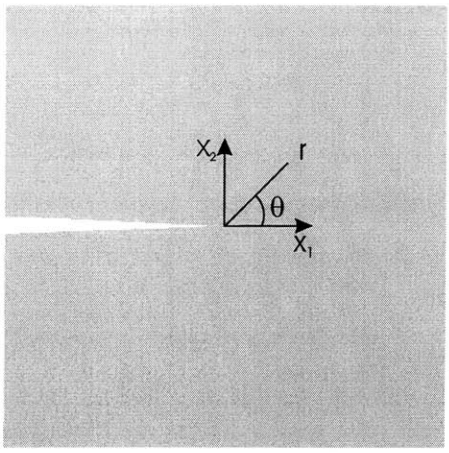

Figure 3-1: Semi-infinite, straight crack in anti-plane strain

3.1.2 Asymptotic Crack Tip Fields (Mode III)

Consider a semi-infinite, straight crack in a state of antiplane strain where a cartesian coordinate system is located at the crack tip (Figure 3-2). The only restriction in antiplane strain is that the relative displacement of the crack faces must vanish as we approach the crack tip. It will also be assumed that the crack faces are traction free. The crack faces considered here are at $\theta = \pi$ and $\theta = -\pi$.

The traction free crack faces boundary condition requires that

$$\sigma_{23} = 0 \; on \; \theta = \pm\pi \tag{3.7}$$

The restriction that the relative displacement vanish at the crack tip is satisfied, and the rigid-body translation of the body is fixed, by requiring the displacement field to vanish at the crack tip,

$$\lim_{|x|\to 0} u_3 = 0. \tag{3.8}$$

The objective is to find the most general form of the antiplane strain complex potential and of the displacement and stress fields that are consistent with the conditions (3.7) and (3.8). Consider a function of the form

$$\psi(z) = (A + iB)z^{\lambda+1} \tag{3.9}$$

where A, B, and λ are real. Substituting the assumed form (3.9) of the antiplane strain complex potential into the expression (3.5) for the scalar components of the stress field gives

$$\begin{aligned} \sigma_{13} - i\sigma_{23} &= (\lambda + 1)(A + iB)z^{\lambda} \\ &= (\lambda + 1)r^{\lambda}(A + iB)(\cos\lambda\theta + i\sin\lambda\theta), \end{aligned} \tag{3.10}$$

so that the stress component field σ_{23} corresponding to the form (3.9) of the antiplane strain complex potential is

$$\sigma_{23} = -(\lambda + 1)r^{\lambda}(A\sin\lambda\theta + B\cos\lambda\theta).$$

The traction-free crack faces boundary condition $\sigma_{23} = 0$ on $\theta = \pm\pi$ requires that

$$\begin{aligned} A\sin\lambda\pi + B\cos\lambda\pi &= 0 \\ -A\sin\lambda\pi + B\cos\lambda\pi &= 0. \end{aligned}$$

The displacement field must vanish at the crack tip and that condition can only be satisfied for $\lambda > -1$. The general solution to the antiplane strain crack problem can them be given in the power series representation

$$\psi(z) = \sum_{n=0}^{\infty} \left[iB_n^{(1)} z^{n+\frac{1}{2}} + A_n^{(2)} z^{n+1} \right] \tag{3.11}$$

where the constant, real coefficients $B_n^{(1)}$ and $A_n^{(2)}$ are determined by the remaining boundary conditions of whatever specific problem one is considering.

As we approach the crack tip, the lower order terms become dominant. The contribution to the stress field, ψ' (Equation 3.6), becomes unbounded for the term $z^{n+1/2}$ at $n = 0$, and provides the most significant contribution when the constant $A_0^{(2)} = 0$. The convention in linear elastic fracture mechanics is to replace the constant $B_0^{(1)}$ by the mode III stress intensity factor K_{III} [19], defined in the cartesian coordinate system such that

$$K_{III} \equiv \lim_{r \to 0} \sqrt{2\pi r}\, \sigma_{23}|_{\theta=0}. \tag{3.12}$$

For this case, Equations (3.5) and (3.10) become

$$u_3 = \frac{2K_{III}}{\mu}\sqrt{\frac{r}{2\pi}}\sin\frac{\theta}{2}, \tag{3.13}$$

and

$$\left\{ \begin{array}{c} \sigma_{13} \\ \sigma_{23} \end{array} \right\} = \frac{K_{III}}{\sqrt{2\pi r}} \left\{ \begin{array}{c} -\sin\frac{\theta}{2} \\ \cos\frac{\theta}{2} \end{array} \right\} \tag{3.14}$$

respectively. The Mode III stress intensity factor is established by the far field boundary conditions and is a function of the applied loading and the geometry of the cracked body. The stress components of Equation (3.14) have an inverse square root singularity at the crack tip and will dominate as the tip is approached. In the limit $r \to 0$, the stress field for any antiplane crack, regardless of the remaining boundary conditions, approaches (3.14) asymptotically. The antiplane crack face relative displacement is

$$\boldsymbol{\delta}(r) \equiv \mathbf{u}(r,\pi) - \mathbf{u}(r,-\pi); \qquad \delta_3(r) \equiv u_3(r,\pi) - u_3(r,-\pi).$$

It follows from (3.13) that

$$\delta_3(r) = \frac{4K_{III}}{\mu}\sqrt{\frac{r}{2\pi}} \tag{3.15}$$

3.1.3 Asymptotic Crack Tip Fields (Modes I and II)

Consider a semi-infinite, straight crack in a state of plane strain, where the cartesian coordinate system is located at the crack tip (Figure 3-2). The only restrictions are that the crack faces should not overlap one another (the crack can "open", but the material on one side cannot penetrate the material on the other side) and that the relative displacement of the crack faces must vanish as one approaches the crack tip. It will also be assumed that the crack faces are traction-free. The crack faces considered here at $\theta = \pi$ and $\theta = -\pi$.

The traction-free crack faces boundary condition requires that

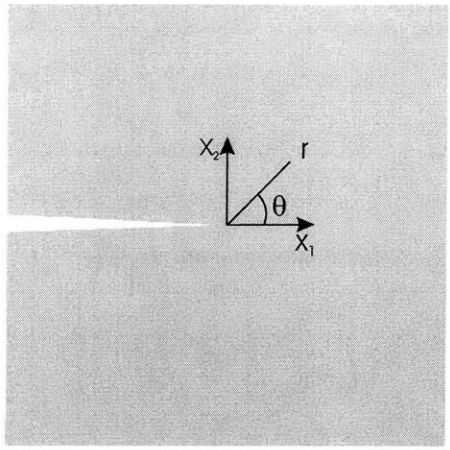

Figure 3-2: Semi-infinite, straight crack in plane strain/stress

$$\sigma_{22} = \sigma_{12} = 0 \text{ on } \theta = \pm\pi. \tag{3.16}$$

In terms of crack relative displacement, the restriction that the relative displacement vanish at the crack tip is satisfied, and the rigid-body translation of the body is fixed, by requiring the displacement field to vanish at the crack tip

$$\lim_{|z|\to 0} \mathbf{u} = \mathbf{0}. \tag{3.17}$$

The objective here is to find the most general forms of the complex stress functions and of the displacement and stress fields that are consistent with the conditions (3.16) and (3.17).

The equilibrium conditions will be satisfied if the nonzero stress components - at points where the body force field is zero - are expressed in terms of the Airy stress function, $\Phi(X_1, X_2)$, such that

$$\sigma_{11} = \Phi_{,22}\,; \quad \sigma_{22} = \Phi_{,11}\,; \quad \sigma_{12} = -\Phi_{,12}\,. \tag{3.18}$$

This guarantees that the two nontrivial equilibrium equations $\sigma_{\alpha\beta,\alpha} = 0$ are satisfied. The equation of elasticity that remains to be satisfied is the compatibility condition, which is given in terms of the Airy stress function by

$$\nabla^4\Phi = 0. \tag{3.19}$$

Thus the Airy stress function must be biharmonic in any region where the body force field is zero. It can be shown that in a region $\mathcal{S}$ where the body force field is zero, every Airy stress function Φ that satisfies the compatibility condition $\nabla^4\Phi = 0$ can be represented in $\mathcal{S}$ by

$$\Phi = \Re\left\{\bar{z}\phi(z) + \Psi(z)\right\}, \tag{3.20}$$

where $\phi(z)$ and $\Psi(z)$ are analytic in $\mathcal{S}$. The scalar components of stress in terms of the complex stress functions can be given by

$$\sigma_{22} + i\sigma_{12} = 2\Re\left(\phi'\right) + \bar{z}\phi'' + \psi'. \tag{3.21}$$

The boundary condition 3.16 requires that $\sigma_{22} + i\sigma_{12} = 0$ on $\theta = \pm\pi$.

For plane strain, the constitutive equations can be rewritten as

$$\sigma_{\alpha\beta} = 2\mu\left[\varepsilon_{\alpha\beta} + \frac{3-\kappa}{2(\kappa-1)}\varepsilon_{\gamma\gamma}\delta_{\alpha\beta}\right], \tag{3.22}$$

where the material property κ is given by $\kappa = 3 - 4\nu$. It follows from Equation (3.22) and strain-displacement relation that

$$\sigma_{11} + \sigma_{22} = \frac{4\mu}{\kappa-1}(u_{1,1} + u_{2,2})$$

and thus it can be shown that the scalar components of displacement are [18]

$$2\mu(u_1 - iu_2) = -\bar{z}\phi' + \kappa\bar{\phi} - \psi. \tag{3.23}$$

Consider two functions of the form

$$\phi = Az^{\lambda+1},\ \psi = Cz^{\lambda+1} \tag{3.24}$$

where A, B, and λ are real. Substituting Equation (3.24) of the complex stress functions into the expression (3.21) and using Euler's formula to separate the real

and imaginary parts gives:

$$\sigma_{22} + i\sigma_{12} = (\lambda + 1)\ r^{\lambda}\ ((2A\cos\lambda\theta + A\lambda\cos(\lambda - 2)\theta + B\cos(\lambda\theta)) \\ +i(A\lambda\sin(\lambda - 2)\theta + B\sin(\lambda\theta))). \tag{3.25}$$

It follows that the traction-free crack faces boundary condition requires

$$\begin{aligned} A(2 + \lambda)\cos\lambda\pi + B\cos(\lambda\pi) = 0 \\ A\lambda\sin(\lambda\pi) + B\sin(\lambda\pi) = 0. \end{aligned} \tag{3.26}$$

The non-trivial solutions to Equation (3.26) can be given by $\lambda > -1$. The general solution to the crack problem can then be given in a power series representation:

$$\begin{aligned} \phi = \textstyle\sum_{n=0}^{\infty} \left[A_n^{(1)} z^{n+\frac{1}{2}} + A_n^{(2)} z^{n+1}\right] \\ \psi = \textstyle\sum_{n=0}^{\infty} \left[B_n^{(1)} z^{n+\frac{1}{2}} + B_n^{(2)} z^{n+1}\right] \end{aligned} \tag{3.27}$$

The constant, real coefficients $A_n^{(1)}$, $B_n^{(1)}$,$A_n^{(2)}$,$B_n^{(2)}$ are determined by the remaining boundary conditions of the specific problem.

The terms in z provide a constant contribution to the stress and the terms in $z^{1/2}$ provide a contribution that becomes unbounded like $|z|^{-1/2}$. The dominant contribution to the crack tip stress and displacement fields occurs for $\lambda = -1/2$, where $n = 0$ for which $A_0^{(1)} = 2B_0^{(1)}$. An inverse square root singularity exists at the crack tip and the scalar components of stress in terms of the complex stress functions (Equation 3.21) become unbounded, defining mode I fields.

The procedure can be repeated for solutions of the form

$$\phi = Az^{\lambda+1},\ \psi = Bz^{\lambda+1} \tag{3.28}$$

but this time with pure imaginary coefficients A and B to define the Mode II fields. As a last step, the two solutions can be superimposed to result in the definition

$$K_I + iK_{II} \equiv \lim_{r\to 0} \sqrt{2\pi r}(\sigma_{22} + i\sigma_{12})|_{\theta=0}. \tag{3.29}$$

Hence, the contribution to the stress field defined by Equation 3.21 can be shown [18] to take the form

$$\left\{ \begin{array}{c} \sigma_{11} \\ \sigma_{22} \\ \sigma_{12} \end{array} \right\} = \frac{K_I}{4\sqrt{2\pi r}} \left\{ \begin{array}{c} 3\cos\frac{\theta}{2} + \cos\frac{5\theta}{2} \\ 5\cos\frac{\theta}{2} - \cos\frac{5\theta}{2} \\ \sin\frac{5\theta}{2} - \sin\frac{\theta}{2} \end{array} \right\} + \frac{K_{II}}{4\sqrt{2\pi r}} \left\{ \begin{array}{c} -5\sin\frac{5\theta}{2} - 7\sin\frac{\theta}{2} \\ \cos\frac{5\theta}{2} - \sin\frac{\theta}{2} \\ 3\cos\frac{\theta}{2} + \cos\frac{5\theta}{2} \end{array} \right\} \quad (3.30)$$

In the limit $r \rightarrow 0$ as one approaches the crack tip, the stress field for any plane strain/stress crack, regardless of the remaining boundary conditions, asymptotically approaches Equation (3.29).

Finally, the contribution to the displacement field is given in terms of cartesian coordinate scalar components by

$$\left\{ \begin{array}{c} u_1 \\ u_2 \end{array} \right\} = \frac{K_I}{2\mu}\sqrt{\frac{r}{2\pi}}\,(\kappa - \cos\theta) \left\{ \begin{array}{c} \cos\frac{\theta}{2} \\ \sin\frac{\theta}{2} \end{array} \right\} + \frac{K_{II}}{2\mu}\sqrt{\frac{r}{2\pi}} \left\{ \begin{array}{c} (2+\kappa+\cos\theta)\sin\frac{\theta}{2} \\ (2-\kappa-\cos\theta)\cos\frac{\theta}{2} \end{array} \right\} \quad (3.31)$$

The crack front relative displacement $\boldsymbol{\delta} = \delta_\alpha \hat{\mathbf{e}}_\alpha$ is the displacement discontinuity across the crack (Figure 3-2), given as a function of the distance r from the crack tip by

$\boldsymbol{\delta}(r) \equiv \mathbf{u}(r,\pi) - \mathbf{u}(r,-\pi)$ Hence from Equation (3.31),

$$\delta_1(r) = K_{II}\,\frac{\kappa+1}{\mu}\sqrt{\frac{r}{2\pi}} \quad (3.32)$$

and

$$\delta_2(r) = K_I\,\frac{\kappa+1}{\mu}\sqrt{\frac{r}{2\pi}}. \quad (3.33)$$

Chapter 4

Modelling, Analysis, and Results

Two models are examined using ABAQUS Standard, Version 6.3-1. The input files for ABAQUS were created using a mesh generation code created in MATLAB[1].

4.1 Modelling

The specimens to be simulated are $3-D$ center cracked specimens of finite dimensions (Figure 4-1). The first specimen (Figure 4-1 (a)) has a flat crack while the crack in the second specimen (Figure 4-1 (b)) has the form of a sinusoid to represent a surface roughness. Utilizing the symmetry on the $Y-Z$ plane, only half of the specimens will be modelled in the finite element analysis (Figure 4-2). Modelling required decision making on three fronts: Boundary conditions, dimensions, and meshing decisions. Each criterion will be discussed in detail in this section.

4.1.1 Setup and Boundary Conditions

Both setups (Figure 4-2) are modelled as linear elastic, using 27-node full integration hexahedral elements (ABAQUS Element Type C3D27). The mesh is created on the $X-Y$ plane and extruded into the $+Z$-direction from $Z=0$ to $Z=Z_{max}$ as stated by the right hand rule. Taking Figure 4-2(a) as a reference, the global cartesian

[1]The MATLAB code is discussed in detail in Appendix A.

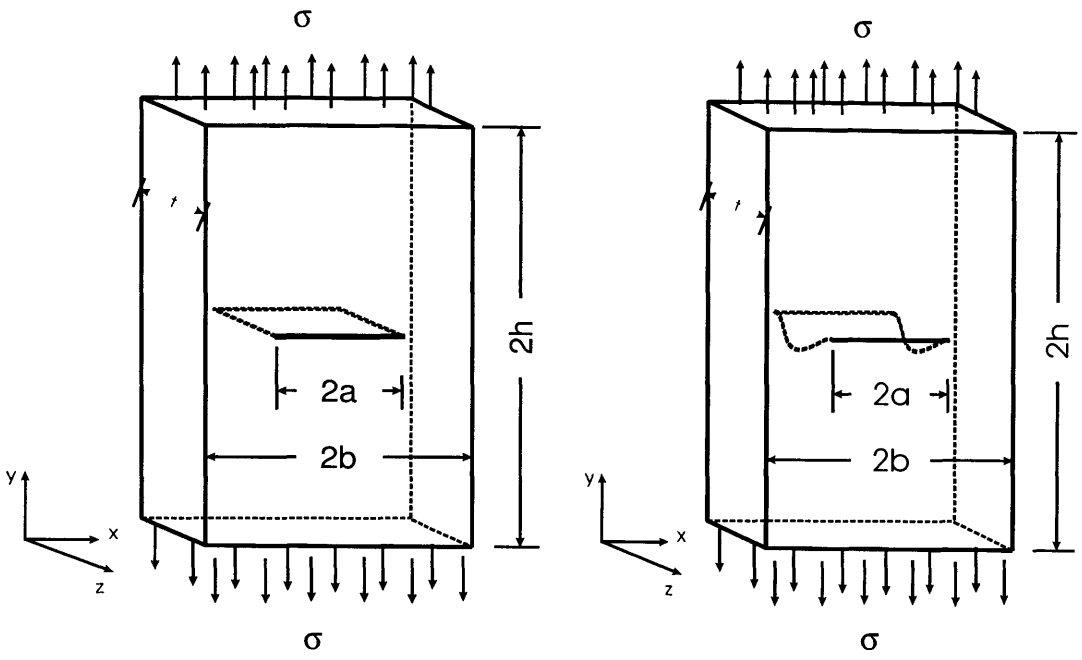

Figure 4-1: Plot of the through crack specimen modelling a (a) flat crack (b) surface roughness.

coordinate system has its origin at the start of the crack on the $Y - Z$ plane and at the mirror image position for the $X - Z$ plane. Both specimens are center-cracked, finite-width test specimens as shown in Figure 4-1. Therefore, in the FEM model, the specimen surface parallel to the $Y - Z$ plane at $X = 0$ is on rollers. At $X = X_{max}$, the surface lying on the $Y - Z$ plane is traction free. The models assume traction-free crack faces, and plane strain in the finite thickness of the specimen. Therefore, movement in the Z-direction on faces lying on the $X - Y$ plane, namely at $Z = 0$ and $Z = Z_{max}$, is fixed. The load is normal traction applied perpendicular to the $X - Z$ plane at $Y = +Y_{max}$ and $Y = -Y_{max}$. The only difference between the two setups is that the specimen in Figure 4-2(a) has a flat crack, where as the crack in Figure 4-2(b) is modelled as a cosine function of one full cycle - with no phase shift - on the $Y - Z$ plane, having a user-defined amplitude, Amp. Hence, the first setup is a special case of the second setup with $Amp = 0$. Even though the models look similar, the flat crack produces pure mode I stress intensity factors, while the out-of-plane crack on the second model results in variable mixed-mode stress intensity factors as

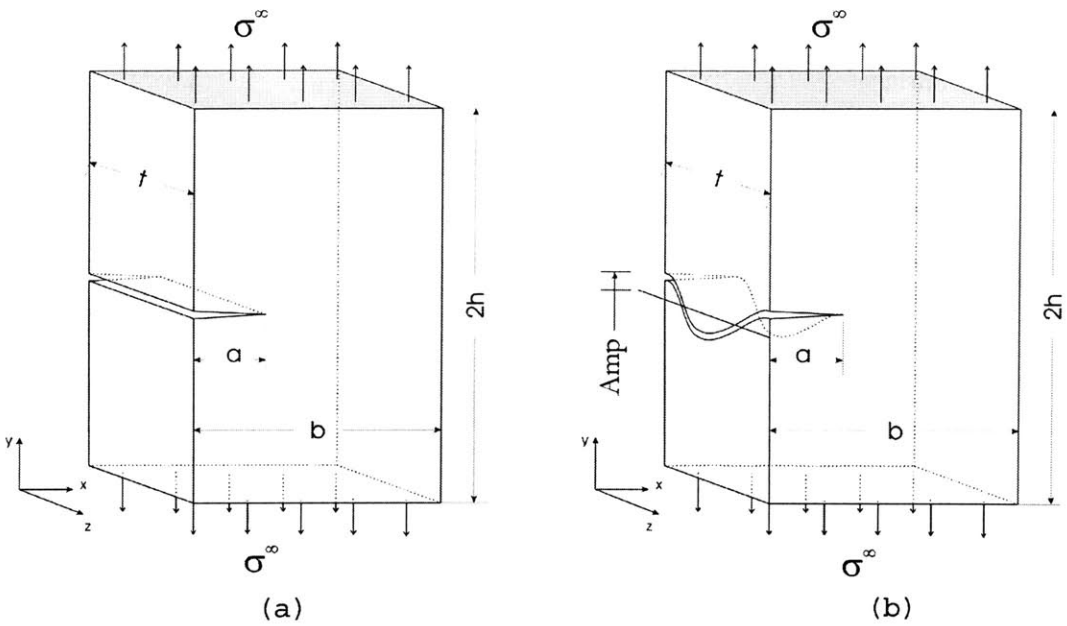

Figure 4-2: Plots of (a) flat and (b) sinusoidal crack geometries. *Note*: The plane $X = 0$ is assumed to be a symmetry plane in both geometries.

we move along the sinusoidal crack front. The load at $Y = Y_{max}$ remains identical in both cases.

4.1.2 Dimensions of the Test Specimen

Even though the ideal analytical model assumes an infinitely long specimen in the Y-direction, a few practical decisions had to be made for the finite element model setup. *Saint-Venant's principle* states that the effect of change in boundary conditions is local. Therefore, sufficiently far from the part of the boundary where the conditions are different, the solutions to infinite-size and finite-size problems are expected to be approximately the same. The problem now is to determine "sufficiently far". For this purpose, simulations were run with different sets of specimen dimensions, and a ratio of $b/h = 1/3$ was selected. We considered the ratio of specimen thickness, t, to the crack amplitude, Amp, a critical one for our calculations. As the elements along the sinusoidal crack front would be distorted, and as excessively distorted elements could lead to inaccurate results, we selected a low ratio of $Amp/t = 1/20$. The crack front

	(a)	(b)
$\frac{a}{b}$	$\frac{1}{4}$	$\frac{1}{4}$
$\frac{a}{t}$	$\frac{1}{2}$	$\frac{1}{2}$
$\frac{b}{h}$	$\frac{1}{3}$	$\frac{1}{3}$
$\frac{Amp}{t}$	0	$\frac{1}{20}$

Table 4.1: Dimensions of the specimens (Figure 4-2 (a),(b)) in relative terms.

consists of the arc length created by the cosine-shaped curve. The mesh is created by linearly spacing the elements along the Z-coordinate and then distorting the crack to accommodate for any given amplitude Amp. Therefore, as the amplitude is increased, the elements at the steepest parts of the curve would have significantly larger arc-length per element and not capture critical information. A low Amp/t ratio thereby determines a sufficiently small maximum "arc length per element" value. With the selected Amp/t ratio, we hope to achieve good numerical results for a computationally affordable price. The relative dimensions of the specimens are given in Table 4.1. The Poisson's ratio was taken as $\nu = 0.3$.

4.1.3 Meshing

The mesh geometry near the crack tip is crucial to obtain an accurate reading of the desired parameters. The computational aspects of creating the mesh have been discussed in detail in Appendix A. This section discusses the reasoning behind the meshing decisions. A schematic of the mesh used in this model has been given in Appendix A, Figure A-1 (a). The mesh for the specimen consists of eight sections, four of which are unique and mirror-imaged across the $X - Z$ plane to result in eight subsections. The sections are then tied to each other using linear multi-point constraints. The sections surrounding the crack front (Section 1 and Section 8) are discussed here in detail. In LEFM analysis, the singularity at the crack front must

be considered, since including the singularity effect around the crack tip improves the accuracy of the computed J-Integral, the stress intensity factors, and the stress and strain calculations[2]. Figure 4-3 illustrates the collapse of a two-dimensional element and the rearrangement of mid-side nodes to capture the crack-tip singularity. The same procedure can be applied to the 27-node $3-D$ hexahedral elements used in our models. To obtain a combined square root and $1/r$ singularity, the nodes on the collapsed face are allowed to displace independently at the crack-tip and the mid side nodes are moved to the 1/4 point. To obtain accurate results, the number of circumferential elements were selected to give subtended angles of less than 10° at the crack-tip. The nodes are radially biased towards the crack tip (Figure 4-4) to make more efficient use of the elements in the model by including more elements in the K-dominated zone. Hence, the characteristic radial lengths of the first few rings of elements around the crack-tip are smaller than they would have been if they were linearly distributed. The uniformly-spaced mesh (Figure 4-4(a)) places all mid-side nodes at the middle of the element, while the quadratic biasing factor (Figure 4-4(b)) forms the first ring of elements as quarter-point elements, and places the mid-side nodes of the remaining layers farther away from the quarter-point location and closer to mid-point.

Another critical decision was selecting the number of elements in the Z-direction, across the thickness, to accommodate the deformation in the sinusoidal crack front, as described in Section 4.1.2. We decided to place 20 elements through the thickness. This made the finite element analysis computationally feasible while providing accurate results for the tested Amp/t range. Coupled with the 'crack amplitude to thickness ratio' decision, the choice of characteristic element size in the first tube of elements along the crack front is expected to provide good results. Table 4.2 presents the ratios selected on meshing the specimen dimensions. The characteristic size in R-direction for Section 1 gives the size of the first element ring around the crack tip relative to the crack length. Due to the biasing algorithm, this ratio is larger as we move farther away from the crack tip.

[2]Please refer to ABAQUS manual [20], Section 7.9.2.

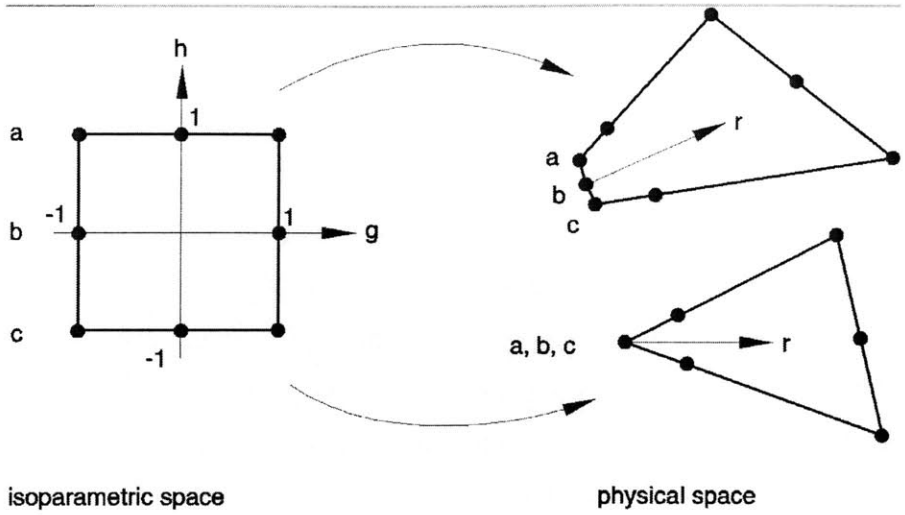

Figure 4-3: Collapsed $2-D$ element used at crack-tip. The variable r is the distance from the crack-tip. In the physical space, the boundary nodes are located 1/4 of the distance from the tip cluster (a,b,c) to the opposite face.

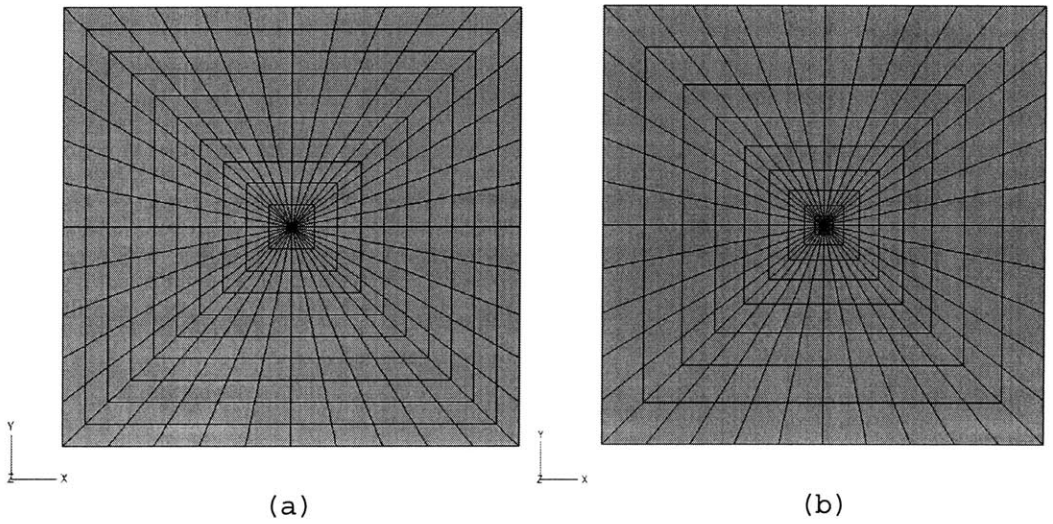

Figure 4-4: Mesh near crack tip for different radial biasing coefficients (b.c) (a) b.c=1 (no 1/4-point elements); (b) b.c=2 (with 1/4-point elements). In both meshes 10 rings of elements are shown.

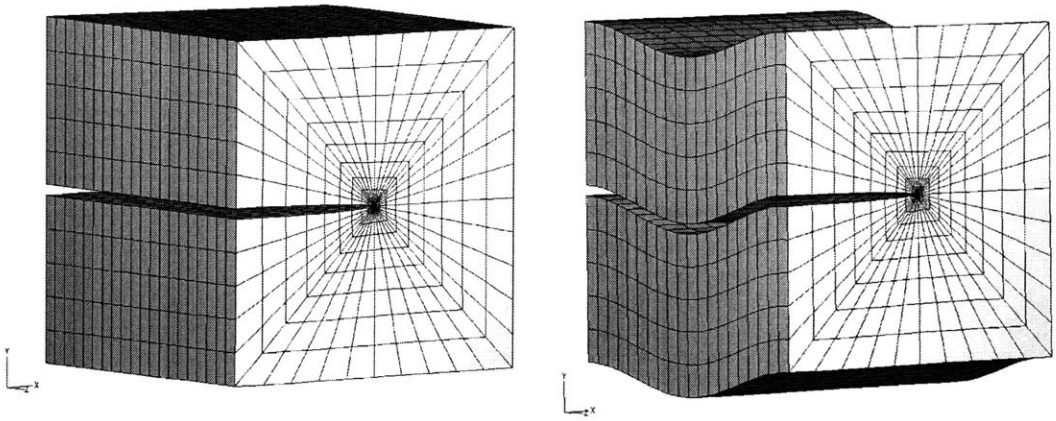

Figure 4-5: Deformed view of mesh near crack tip for (a) flat crack (b) sinusoidal crack.

Section		Extent of Dimension	Number of Elements	Characteristic Size
1	R	5	10	1/100
	θ	180^0	20	9^0
	Z	10	20	1/2
2	X	10	10	1
	Y	55	5	11
	Z	10	20	1/2
3	X	10	5	2
	Y	55	5	11
	Z	10	20	1/2
4	X	10	5	2
	Y	5	5	1
	Z	10	20	1/2

Table 4.2: Number of elements used in each of the four unique sections for modelling and the characteristic sizes corresponding to the specimen dimensions. For length-dimensioned parameters, the absolute dimensions are arbitrary.

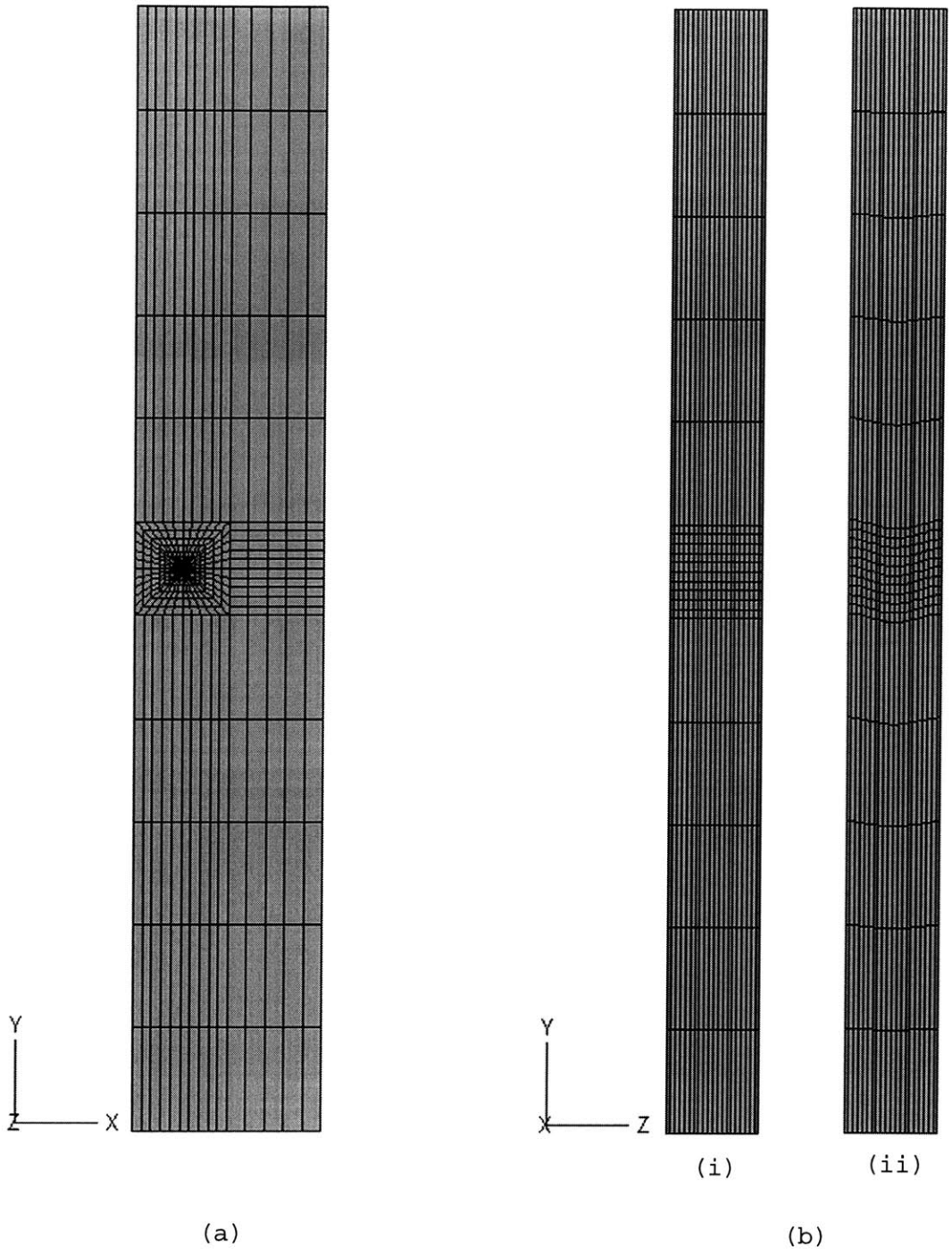

Figure 4-6: Plot of meshes tested (a) View in X-Y plane (b) View in Y-Z plane for (i) flat crack; (ii) sinusoidal crack ($Amp/t = 1/20$).

4.2 Analysis

The goal of the simulations is to study the behavior of the stress intensity factors as we move along the crack front from $Z = 0$ to $Z = Z_{max}$ in different crack front geometries. ABAQUS writes its findings to the .dat output file, but they need to be post-processed and formatted to serve our purposes. First, we ran the MATLAB post-processing code written for this purpose[3]. Second, using the crack face displacements, we calculated the stress intensity factors from CFRD. Finally, all data is normalized by the reference solutions obtained from an engineering handbook [21] corresponding to the load characteristics and plotted against Z. In other words, the final product of postprocessing is plots of normalized singularity strengths (K_I, K_{II}, K_{III}, J) obtained from the interaction integral method. Each plot contains two set of values, representing two contours. This serves to test the path independence. To verify the accuracy of the results, stress intensity factors calculated using the CFRD methodology are superimposed on those existing K_I, K_{II}, and K_{III} plots, while the direct calculation of the J-Integral was superimposed on its counterpart that was calculated from the stress intensity factors.

The first model is the flat crack: This model was included to test the accuracy of the pre- and postprocessing algorithms, including meshing. The expected outcome of the analysis under the specified load is a normalized K_I value of unity, and zero K_{II} and K_{III} values.

For the sinusoidal crack, we expect the stress intensity factors to vary as we move along the sinusoidal crack front. K_I is predicted to be highest at the points where the crack resembles a pure mode I setup, namely at the maximum and minimum values of the cosines curve. Conversely, K_I should be lowest where the sinusoidal curve is steepest. The steepest sections are also expected to correspond to highest K_{III} contribution. Therefore, K_I is expected to reach its maximum at $Z = 0$, $Z = 1/2\, Z_{max}$, and $Z = Z_{max}$ and to have a minimum at $Z = 1/4\, Z_{max}$ and $Z = 3/4\, Z_{max}$. K_{III} is expected to reach its highest magnitude at $Z = 1/4\, Z_{max}$ and at $Z = 3/4\, Z_{max}$.

[3]Please refer to Appendix A for a detailed discussion of the postprocessing codes

	Magnitude	$Z = 0$	$Z = \frac{1}{4} Z_{max}$	$Z = \frac{1}{2} Z_{max}$	$Z = \frac{3}{4} Z_{max}$	$Z = Z_{max}$
K_I	max.	√		√		√
	min.		√		√	
K_{II}	max.	√		√		√
	min.(= 0)		√		√	
K_{III}	max.		√		√	
	min. (= 0)	√		√		√

Table 4.3: Expected locations of largest magnitudes of mixed-mode stress intensity factors along the sinusoidal crack front. Estimations are given in absolute value terms.

From symmetry, we expect K_{II} to be zero at $Z = 1/4\, Z_{max}$ and $Z = 3/4\, Z_{max}$ and to have largest magnitude at $Z = 0$, $Z = 1/2\, Z_{max}$, $Z = Z_{max}$. The expected behaviors of the stress intensity factors along the crack front for the sinusoidal crack have been summarized in Table 4.3, albeit no reference to the sign convention has been made.

4.3 Results

The results for the flat crack are displayed in Figure (4-8). The K_I reading gives an error at an acceptable level of 1%, and is constant across the crack front. Mode II and mode III stress intensity factors are zero throughout, as expected. The J-Integral calculations from two different methods are also in agreement.

When we test the specimen with the out-of-plane sinusoidal crack front, to a certain extent we do observe the expected patterns (Figure 4-9). The interaction integral calculations from crack front nodal locations interior to a set of C3D27 elements (i.e., midplane nodes) are contour-independent and in agreement with the CFRD readings in the case of stress intensity factors and with direct calculations in the case of the J-Integral. Overall, trends are consistent with expectations noted above. However, the readings from crack front corner nodes located at an edgeplane connecting two crack front segments exhibit a curious, contour-dependent behavior. In our setup, midplane nodes are defined as nodes that do not lie on an element edge along the

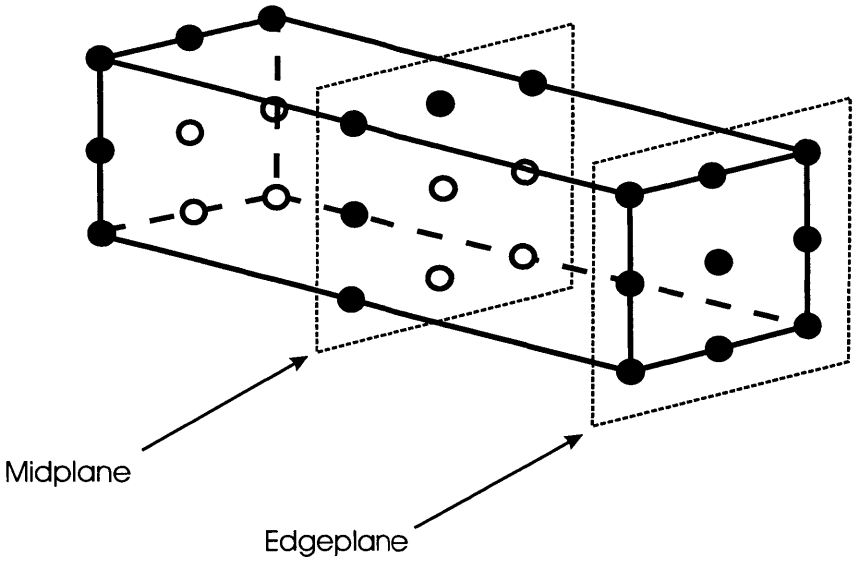

Figure 4-7: Illustrative definition of the terms 'midplane' and 'edgeplane' in three dimensional 27 node hexahedral elements.

crack front. A schematic representation of midplane and edgeplane nodes can be found in Figure (4-7).

Mode I (K_I):

The mode I stress intensity factors show a sinusoidal pattern as we move along the crack front (Figure 4-9 (a)). The readings are in agreement with the predicted pattern. The resulting curve resembles a cosine function in the form

$$K_I = K_I^{(base)} + K_I^{(amp)} \cos(\lambda u + \varphi) \tag{4.1}$$

where $u = 2\pi(Z/Z_{max})$ and serves to map one full cycle along the crack front. The results indicate an amplitude $K_I^{(amp)}$, frequency $\lambda = 2$, and phase shift $\varphi = 0$ in agreement with the predictions in Table 4.3. The amplitude of the function is more difficult to determine. The interaction energy integral readings at midplane nodes along the crack front are contour-independent but seem to be contour-dependent at the edgeplane nodes, especially where the K_I contribution is largest. Interpreted literally, the amplitude of the predicted K_I curve apparently changes as we move away from the crack front. As the contour number increases, i.e., the volume in the integra-

tion grows larger, the edgeplane nodes increasingly lower the amplitude of the best-fit curve $K_I^{(amp)}$. Superimposed CFRD results match with the contour-independent midplane nodes. Moreover, the CFRD results calculated at the edgeplane nodes are consistent with interpolation/extrapolation of the contour-independent pattern of the midplane nodes. However, it is worth noting that the CFRD results are 0.5% lower than the interaction integral mode I calculations at points where the K_I contribution to the crack is least.

Mode II (K_{II}):

The resulting plot, Figure 4-9 (b), resembles a cosine function of the form

$$K_{II} = K_{II}^{(amp)} \cos(\lambda u + \varphi) \tag{4.2}$$

with an amplitude $K_{II}^{(amp)}$, frequency $\lambda = 1$, and phase shift $\varphi = \pi$ in agreement with the predictions in Table 4.3. While the mode II stress intensity factors calculated through the interaction integrals act similarly to their mode I counterparts, the magnitude of contour variation at the edgeplane nodes reaches 40%. Plotting the mode II calculations through CFRD suggests that the contour-independent midplane nodes provide the better solution, as the readings from the two methods agree perfectly.

Mode III (K_{III}):

Mode III stress intensity factors have the form (Figure 4-9 (c))

$$K_{III} = K_{III}^{(amp)} \sin(\lambda u + \varphi) \tag{4.3}$$

with an amplitude $K_{III}^{(amp)}$, frequency $\lambda = 1$, and phase shift $\varphi = \pi$ in agreement with the predictions in Table 4.3. Even though unreliable results from the edgeplane nodes exist in mode III, the variation along the crack front is minimal. The bigger problem seems to be at the ends, at $Z = 0$ and $Z = Z_{max}$, where we observe large jumps of equal magnitude in opposite directions. The magnitude of these jumps at the ends are contour-dependent and reach 40%, twice the amplitude of the sine curve.

***J*-Integral**:

The J-Integral calculations from the interaction energy integrals are arithmetic combinations of the stress intensity factors K_I, K_{II}, and K_{III} and therefore reflect

the same behaviors at the midplane and edgeplane nodes, respectively (Figure 4-9 (c)). J-Integral calculations through interaction integrals are denoted as "II" in the figure, while the direct J-Integral readings calculated through domain integration are referred to as "DI". The direct calculations provide another opportunity to independently verify the inaccuracy of the interaction integral calculations at the edgeplane nodes. The direct J-Integral values are in perfect agreement with the midplane interaction integral calculations. At the edgeplane nodes along the crack front, the directly calculated J's differ from the interaction integral counterparts. The directly-calculated J's at edgeplane nodes are contour-independent and have a value that lies on the same curve set by their midplane counterparts, as calculated using both interaction integral method and direct domain integration methods.

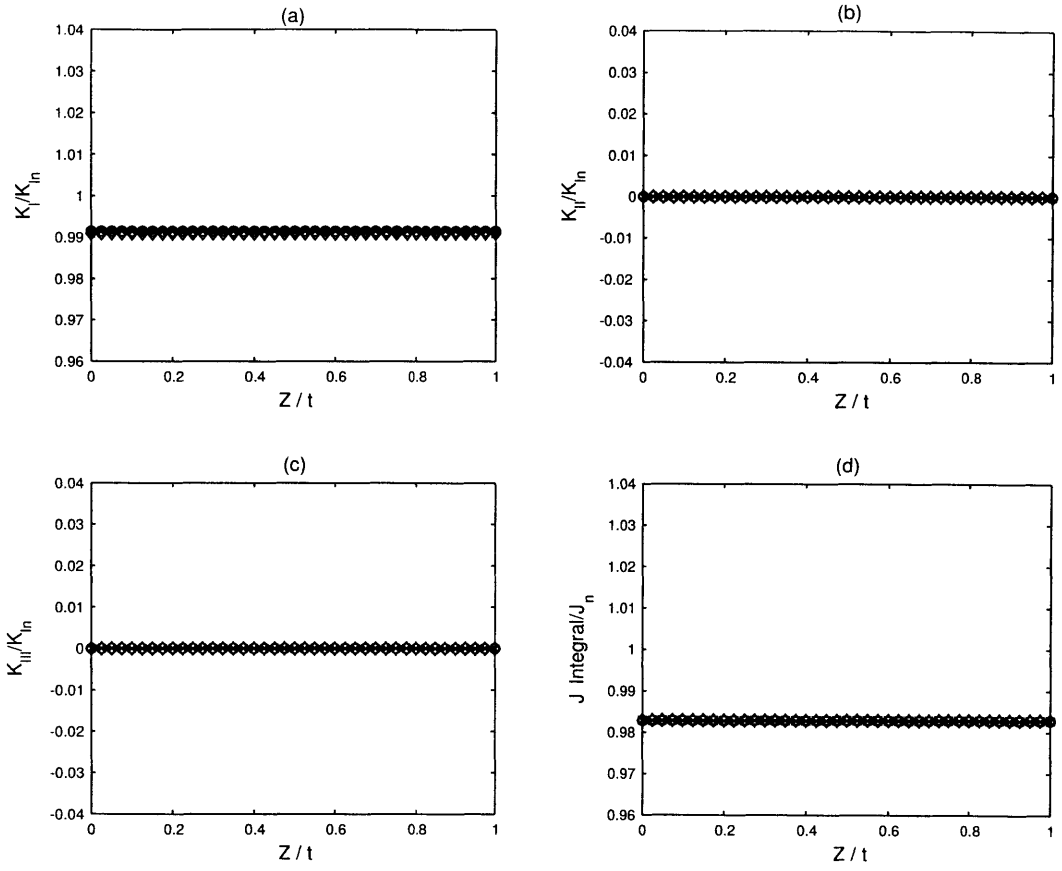

	(a),(b),(c)	(d)
legend	× Contour4 ○ Contour8 ◇ CFRD	× Contour4 (II) ◇ Contour4 (DI) ○ Contour8 (II) □ Contour8 (DI)
normalized by	$K_{I_n} = \sigma\sqrt{\pi a}\ F(a/b)$ $F(a/b) = \frac{1-0.5(a/b)+0.370(a/b)^2-0.044(a/b)^3}{\sqrt{1-(a/b)}}$	$J_n = \frac{K_{I_n}^2}{E/(1-\nu^2)}$

Figure 4-8: Superimposed and normalized (a) K_I (b) K_{II} (c) K_{III} and (d) J-Integral readings for the rectangular specimen with a flat central crack under normal traction load (Plane Strain).

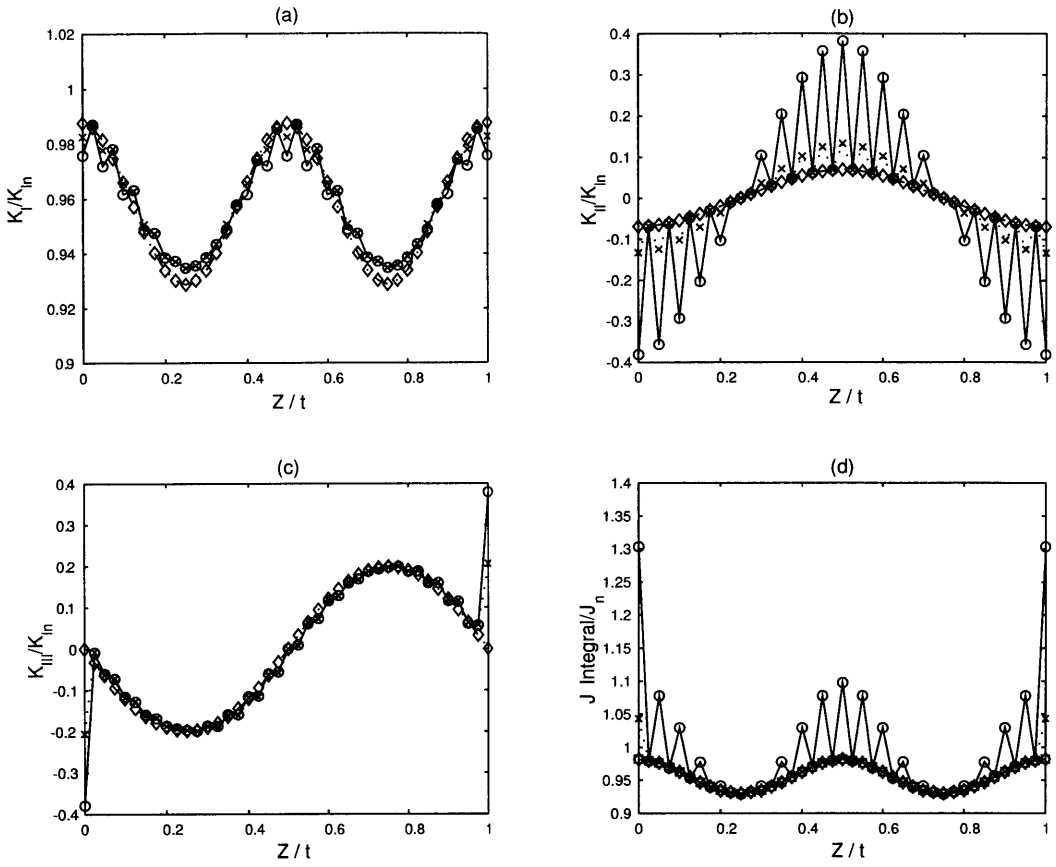

	(a),(b),(c)	(d)
legend	× Contour4 ○ Contour8 ◇ CFRD	× Contour4 (II) ◇ Contour4 (DI) ○ Contour8 (II) □ Contour8 (DI)
normalized by	$K_{I_n} = \sigma\sqrt{\pi a}\,F(a/b)$ $F(a/b) = \frac{1-0.5(a/b)+0.370(a/b)^2-0.044(a/b)^3}{\sqrt{1-(a/b)}}$	$J_n = \frac{K_{I_n}^2}{E/(1-\nu^2)}$

Figure 4-9: Superimposed and normalized (a) K_I (b) K_{II} (c) K_{III} and (d) J-Integral readings for the rectangular specimen with a sinusoidal crack ($Amp/t = 1/20$) under normal traction load (Plane Strain).

Chapter 5

Discussion

While the setup with the flat crack performed as expected, the sinusoidal crack geometry introduced two distinct problems. First, the mode III results have large, contour-dependent jumps at the boundaries $Z = 0$ and $Z = Z_{max}$. These jumps are of opposite sign and of equal magnitude. Second, nodes located at the edgeplane of an element give contour-dependent, inaccurate results for all modes of loading in the interaction integral calculations. The reason for the inaccurate results from ABAQUS is difficult to determine. The ABAQUS theory manual does not detail the steps it takes to form the auxiliary stress and strain fields but the error can be caused by the assumption that the auxiliary stress fields will be divergence free in the absence of body forces. This is a potential source of error as explained in Section 2.2.

The problem of contour-dependent jumps at the boundaries $Z = 0$ and $Z = Z_{max}$ will be examined and discussed in this chapter.

5.1 Boundary Conditions

Even though the readings in the mode II boundary layers at $Z = 0$ and $Z = Z_{max}$ behave the same way, the mode III readings offer the distinct advantage for analysis in that the inaccurate data is limited to the boundaries, and therefore might be isolated easily. To isolate the problem in hand, the boundary conditions for the specimen in the flat crack model have been reset and the finite width center cracked test specimen

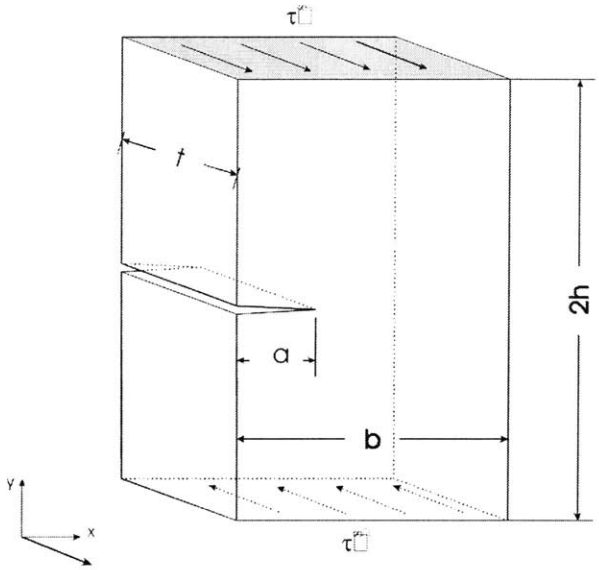

Figure 5-1: Representation of the sheared center cracked specimen to result in pure mode III stress intensity factor.

has been set to result in a pure mode III stress intensity factor (Figure 5-1). The specimen surface on the $Y - Z$ plane at $X = 0$ is again on rollers. At $X = X_{max}$, the surface lying on the $Y - Z$ plane is free. The model assumes traction-free crack faces, motion in any direction other than the antiplane shear direction Z is fixed to obtain a pure mode III loading. The pressure boundary conditions at $Y = Y_{max}$ and $Y = -Y_{max}$ have been replaced with shear tractions τ_{yz}. As ABAQUS cannot directly apply shear tractions to a surface, a uniform displacement in the Z-direction has been applied on the surfaces at $Y = Y_{max}$ and $Y = -Y_{max}$. The resulting shear from the applied displacement has been calculated during postprocessing[1].

The results are plotted in Figure 5-2. The K_I and K_{III} readings behave as expected. K_I has a value of zero across the crack front, while the normalized K_{III} has the constant value of unity. The problem arises in the K_{II} calculations. Mode II stress intensity factor calculations match the expected value of zero, except for at the ends $Z = 0$ and $Z = Z_{max}$. These contour-dependent readings follow a trend similar

[1]For a discussion on how to extract the shear traction from the displacement during postprocessing please refer to Appendix A.

to the K_{III} readings under normal traction load (Figure 4-9 (c)) and are of equal magnitude but of opposite signs. The interaction integral based J-Integral calculations are also affected by this error. Interestingly, unlike in the sinusoidal crack, the error grows larger as the area of integration gets smaller.

As the error at the ends are of the same magnitude but different signs, we model a specimen to simulate periodic boundary conditions. The idea behind this model is to make the faces on the $X - Y$ plane at $Z = 0$ and $Z = Z_{max}$ behave the same way as if they are at the same physical location. We use the same mesh as in Figure 4-2(b) but instead of the plane strain boundary conditions at $Z = 0$ and $Z = Z_{max}$, the specimen is now configured with periodic boundary conditions, as explained in Danielsson, Parks, and Boyce [22]. Our expectation is that the jumps in K_{II} calculated at the ends will "add up" under the periodic boundary conditions and provide us with the correct value of zero.

The results are summarized in Figure 5-3. While the error in the K_{II} readings has been decreased, the results for the edge plane nodes for K_I and K_{III} calculations present even more variation. Moreover, the CFRD readings are higher than the stress intensity factors calculated through the domain integration method for K_I but perfectly match K_{II} and K_{III} at mid plane nodes. The CFRD are expected to provide correct values for the plane strain problem. For the periodic boundary conditions CFRD only provides a qualitative benchmark for the behavior of the mode I stress intensity factors rather than serving as a quantitative comparison tool.

5.2 Alternative Specimen Geometries

Our attempt to make responses at specimen ends "add up and cancel each other" by implementing periodic boundary conditions did not work as implemented. Another option is placing the two faces that are currently at $Z = 0$ and $Z = Z_{max}$ to the same physical location and tying the two faces. This is done by creating a cylindrical specimen instead of a rectangular piece (Figure 5-4). Once the $2 - D$ mesh is

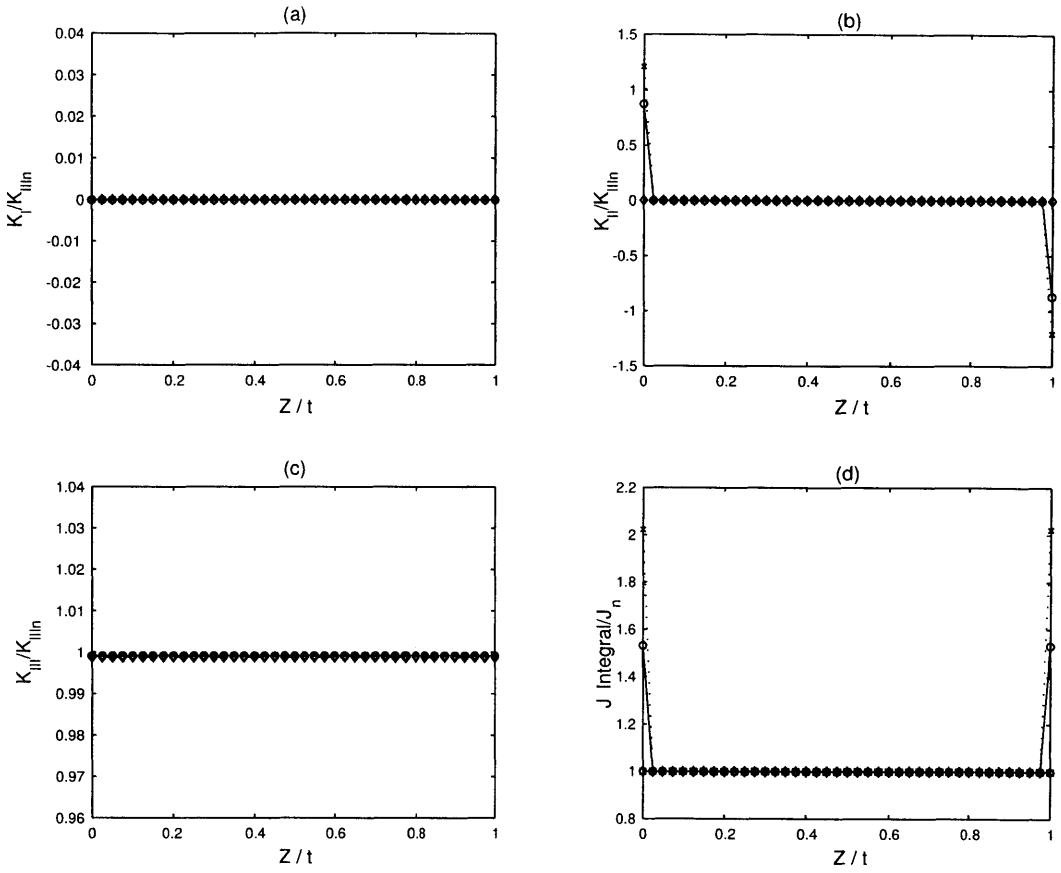

	(a),(b),(c)	(d)
legend	× Contour4 ○ Contour8 ◇ CFRD	× Contour4 (II) ◇ Contour4 (DI) ○ Contour8 (II) □ Contour8 (DI)
normalized by	$K_{III_n} = \tau\sqrt{\pi a}\sqrt{\frac{2b}{\pi a}\tan\frac{\pi a}{2b}}$	$J_n = \frac{K_{III_n}^2}{2G}$

Figure 5-2: Superimposed and normalized (a) K_I (b) K_{II} (c) K_{III} and (d) J-Integral readings for the rectangular specimen with a flat crack under shear load.

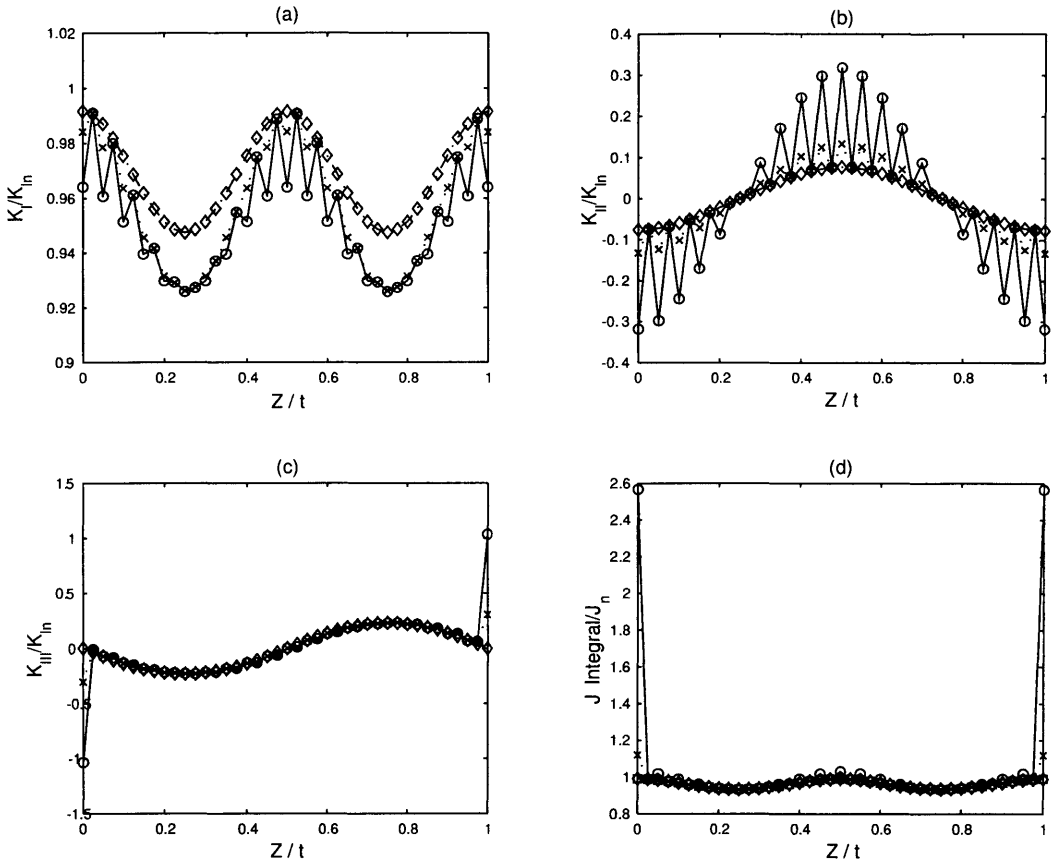

	(a),(b),(c)	(d)
legend	× Contour4 ○ Contour8 ◇ CFRD	× Contour4 (II) ◇ Contour4 (DI) ○ Contour8 (II) □ Contour8 (DI)
normalized by	$K_{I_n} = \sigma\sqrt{\pi a}\ F(a/b)$ $F(a/b) = \frac{1-0.5(a/b)+0.370(a/b)^2-0.044(a/b)^3}{\sqrt{1-(a/b)}}$	$J_n = \frac{K_{In}^2}{E/(1-\nu^2)}$

Figure 5-3: Superimposed and normalized (a) K_I (b) K_{II} (c) K_{III} and (d) J-Integral readings for the rectangular specimen with a sinusoidal crack ($Amp/t = 1/20$) under tension (Periodic Boundary Conditions).

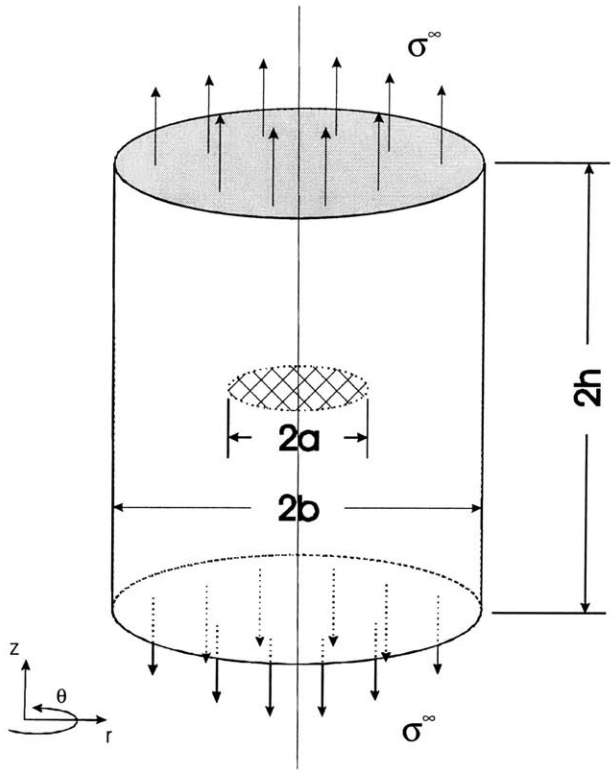

Figure 5-4: Schematic representation of cylindrical bar under normal traction with the penny-shaped crack.

created on the local $X - Y$ plane[2], a cylinder is created by extruding the mesh in the circumferential Θ-direction. The circumference is meshed using 40 elements to reach a subtended angle of 9^o per element - below the 10^o value recommended [20] for accurate results (Figure 5-4). The "ends" of the cylindrical bar at $\Theta = 0$ and $\Theta = 360°$ are tied using linear multi-point constraints. The resulting geometry is a normal traction cylindrical bar with a penny-shaped crack. The only boundary condition applied was normal traction at $Z = Z_{max} = h$ and $Z = -Z_{max} = -h$ on the local cylindrical coordinate system. A reference solution for this problem does exist [21] and is used to normalize the results. We achieve the expected results of unity normalized mode I stress intensity factor along the crack front (circumference) and zero mode II and mode III values (Figure 5-5).

[2]We use the cartesian coordinate system set in Figure 4-9.

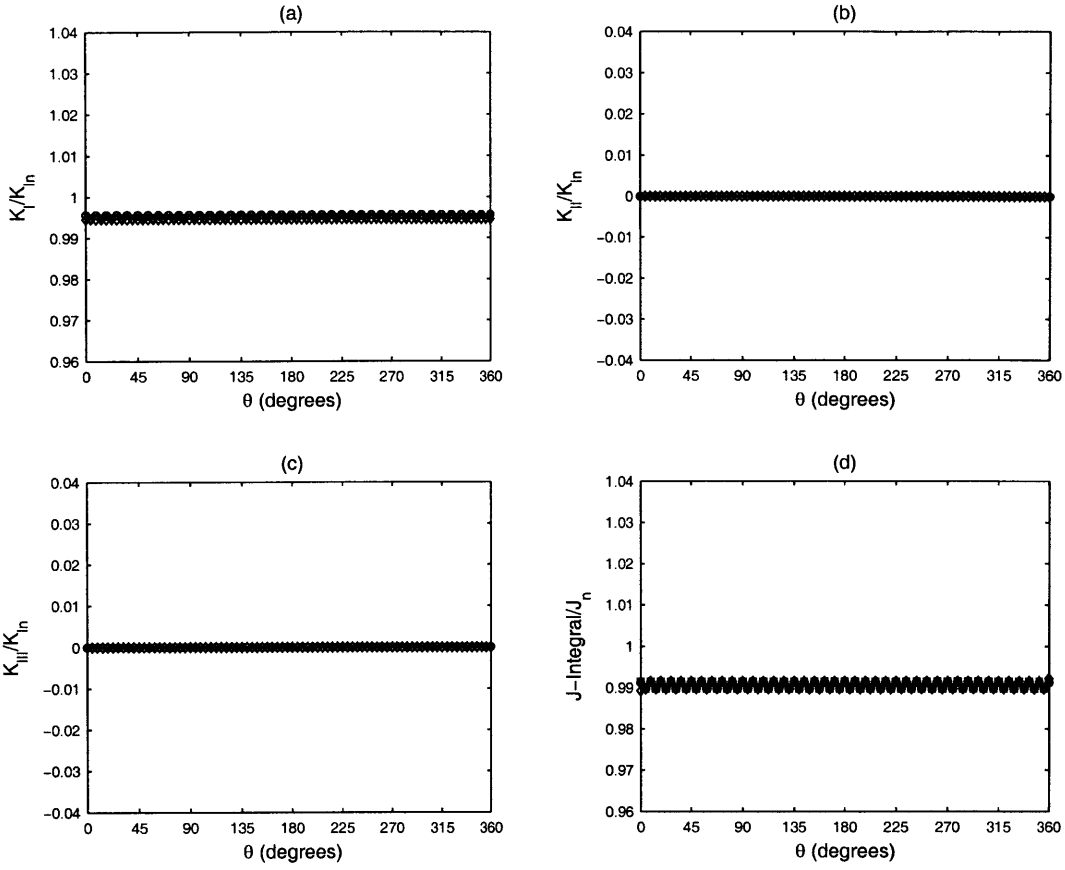

	(a),(b),(c)	(d)
legend	× Contour4 ○ Contour8 ◇ CFRD	× Contour4 (II) ◇ Contour4 (DI) ○ Contour8 (II) □ Contour8 (DI)
normalized by	$K_{I_n} = \frac{2}{\pi}\,\sigma\,\sqrt{\pi a}\;F(a/b)$ $F(a/b) = \frac{1-0.5(a/b)+0.148(a/b)^3}{\sqrt{1-(a/b)}}$	$J_n = \frac{K_{I_n}^2}{E/(1-\nu^2)}$

Figure 5-5: Superimposed and normalized (a) K_I (b) K_{II} (c) K_{III} and (d) J-Integral readings for the cylindrical specimen with a penny-shaped crack under tension.

The cylinder is then tested under torsion (Figure 5-6) to obtain pure mode III stress intensity factors. As ABAQUS cannot directly apply torsion on the specimen, we applied an angular displacement at $Z = Z_{max}$. Degrees of freedom in the Z-direction are fixed for all nodes. During postprocessing the resulting torque due to applied displacement has been calculated as explained in Appendix A. The mode III stress intensity factor did provide its expected value of unity despite some oscillations, possibly due to large subtended angles. We also expected the inaccurate mode II readings that occurred at the ends of the crack front in the rectangular specimen to disappear. As the ends of the cylinder ($\Theta = 0$ and $\Theta = 360°$) lie at the same physical location we expected the readings at the ends to add up and result in the correct value of zero. The new specimen geometry did not solve the problem. The mode II readings at the ends were once again highly inaccurate, leading - for contour 8 - to a 1500% error in the J-Integral calculations from the interaction integrals at the ends (Figure 5-7).

As the problem could not be solved by geometric iteration, we decided to change the definition of the boundaries where the crack front begins and ends. In the standard ABAQUS procedure, all nodes at the crack-tip at any given crack front location are set up as an independent node set. In the case of the cylinder, two node sets exist at the ends, namely at $\Theta = 0$ and $\Theta = 360^o$. The nodes at the ends are then tied using linear multi-point constraints. This way the two faces are forced to move together. For the contour integral calculations in ABAQUS, the user needs to define the node sets that constitute the crack front. In the original cylindrical mesh, a unique node set was described for the 'face' at $\Theta = 0$ and another for the 'face' at $\Theta = 360^o$. We then modified the crack-tip node set definition at these locations. The node sets at these faces are modified to include the other faces' nodes as well. In other words, the crack tip node set at $\Theta = 0$ contains its own nodes as well as the nodes from the crack tip at $\Theta = 360^o$ that are located at the same position, and vice versa. This way, we tested whether the misreadings at the ends will be corrected, as the crack-tip node set at the 'faces' will have their perturbation based on two elements and behave like any other element in the crack front.

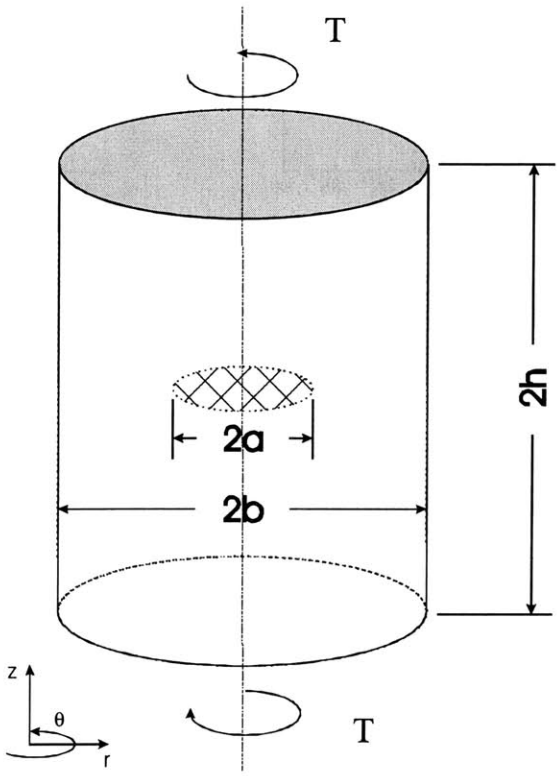

Figure 5-6: Schematic representation of the thick cylindrical specimen under torsion with the penny-shaped crack.

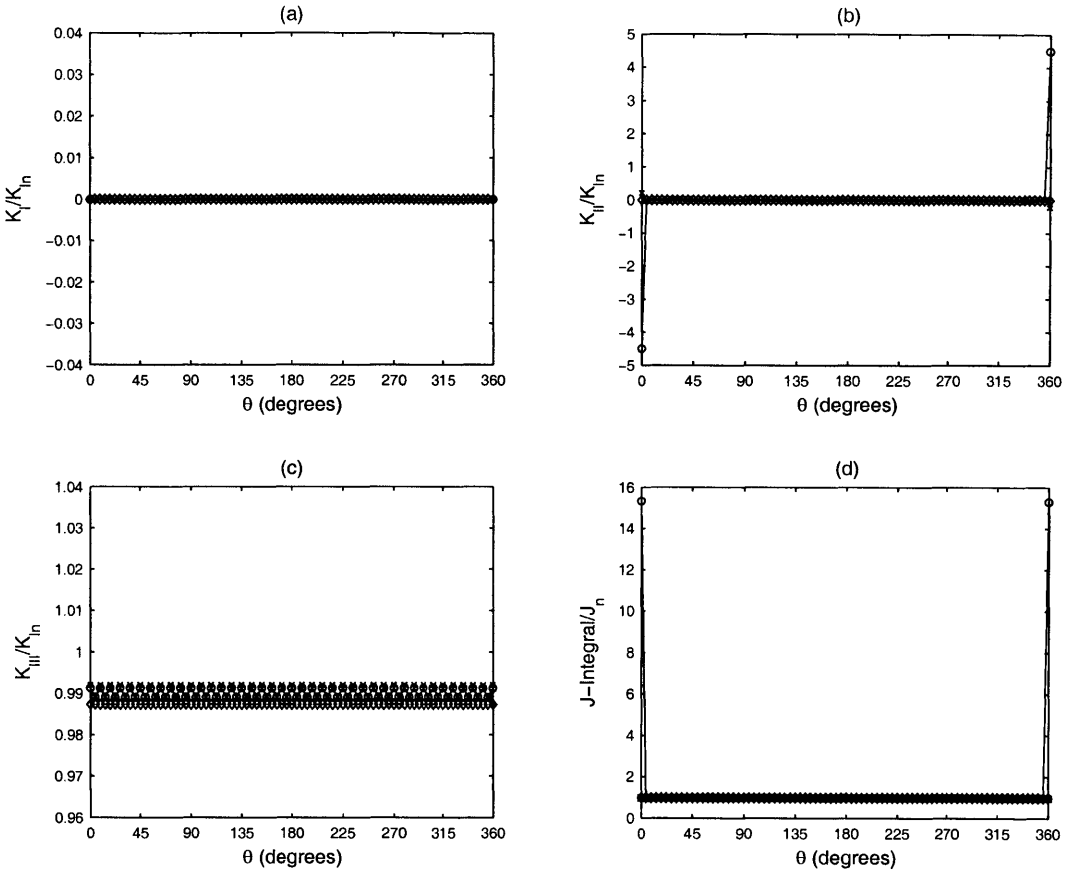

	(a),(b),(c)	(d)
legend	× Contour4 ○ Contour8 ◇ CFRD	× Contour4 (II) ◇ Contour4 (DI) ○ Contour8 (II) □ Contour8 (DI)
normalized by	$K_{III_n} = \tau\sqrt{\pi a}\ G(a/b)\ \sqrt{1-a/b}$ $G(a/b) = \frac{4}{3\pi}\ [1 + 0.5(a/b) + 0.375(a/b)^2$ $+0.3125(a/b)^3 - 0.7266(a/b)^4$ $+0.038(a/b)^5]$	$J_n = \frac{K^2_{III_n}}{2G}$

Figure 5-7: Superimposed and normalized (a) K_I (b) K_{II} (c) K_{III} and (d) J-Integral readings for the cylindrical specimen with a penny-shaped crack under torsion.

The cylinder with the alternative node set definition is first tested under normal traction (Figure 5-8). As expected, the normalized K_I value is near unity, within an acceptable margin of error of 1%, where the stress intensity factors K_{II} and K_{III} are zero. Next, the mesh using the alternative node set definition is tested under torsion (Figure 5-9). The modification in the definition of node sets at the ends has resolved the issue of mode II jumps and the readings present pure mode III results with the remaining stress intensity factors of zero around the circumference (Figure 5-9).

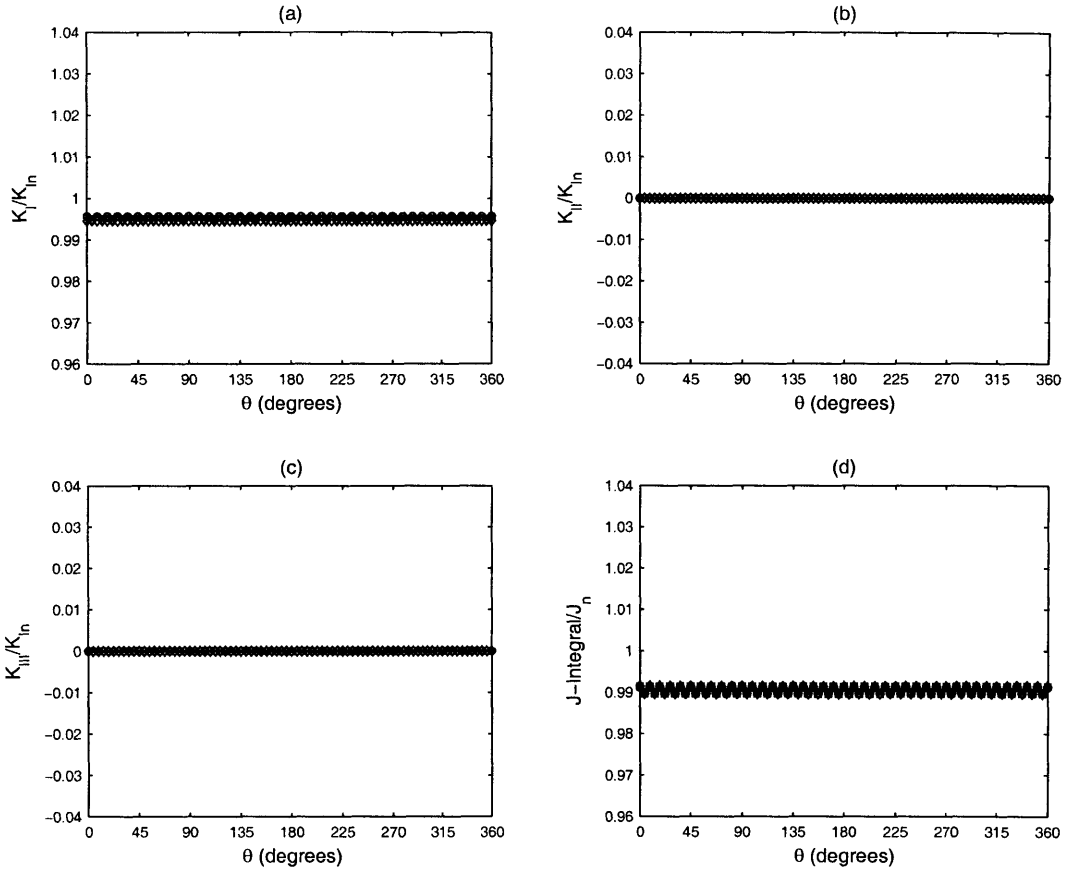

	(a),(b),(c)	(d)
legend	× Contour4 ○ Contour8 ◇ CFRD	× Contour4 (II) ◇ Contour4 (DI) ○ Contour8 (II) □ Contour8 (DI)
normalized by	$K_{I_n} = \frac{2}{\pi}\,\sigma\,\sqrt{\pi a}\;F(a/b)$ $F(a/b) = \frac{1-0.5(a/b)+0.148(a/b)^3}{\sqrt{1-(a/b)}}$	$J_n = \frac{K_{In}^2}{E/(1-\nu^2)}$

Figure 5-8: Superimposed and normalized (a) K_I (b) K_{II} (c) K_{III} and (d) J-Integral readings for the cylindrical specimen with a penny-shaped crack under tension modelled using the alternative node set definition.

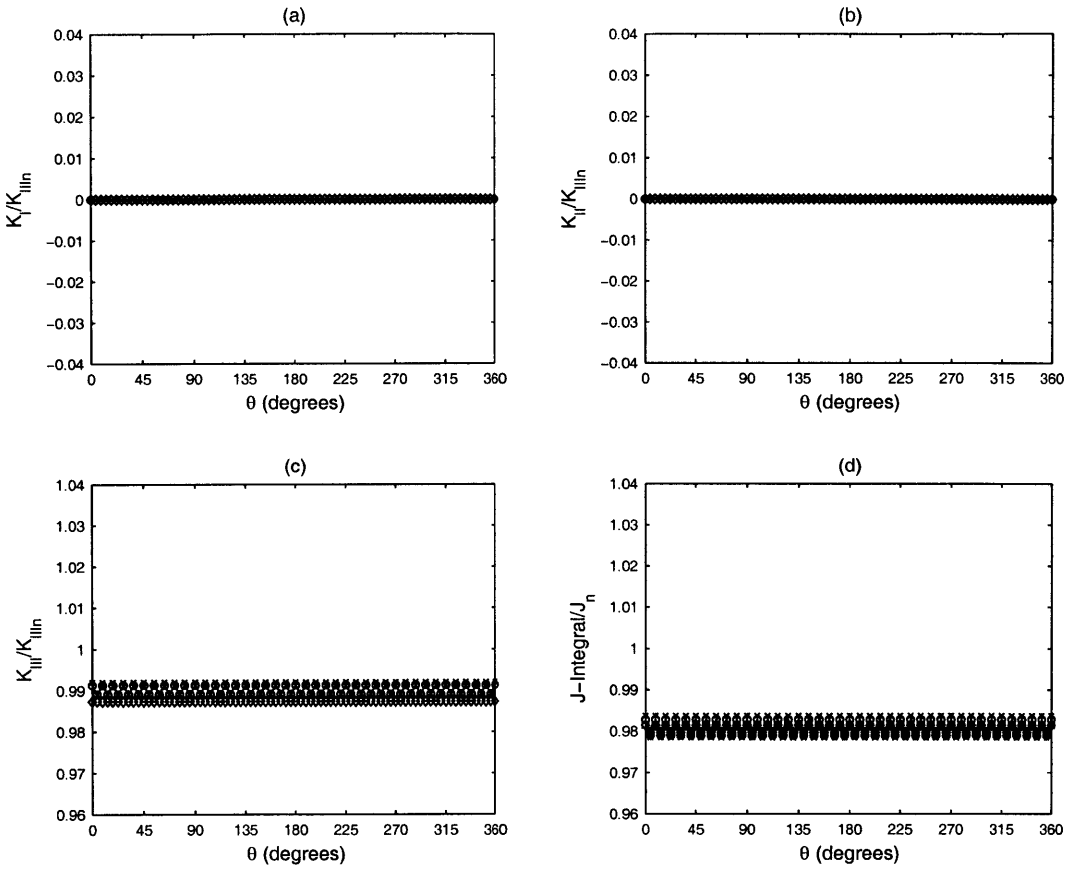

	(a),(b),(c)	(d)
legend	× Contour4 ○ Contour8 ◇ CFRD	× Contour4 (II) ◇ Contour4 (DI) ○ Contour8 (II) □ Contour8 (DI)
normalized by	$K_{III_n} = \tau\sqrt{\pi a}\, G(a/b)\, \sqrt{1-a/b}$ $G(a/b) = \frac{4}{3\pi}\,[1 + 0.5(a/b) + 0.375(a/b)^2$ $+0.3125(a/b)^3 - 0.7266(a/b)^4$ $+0.038(a/b)^5]$	$J_n = \frac{K^2_{III_n}}{2G}$

Figure 5-9: Superimposed and normalized (a) K_I (b) K_{II} (c) K_{III} and (d) J-Integral readings for the cylindrical specimen with a penny-shaped crack under torsion modelled using the alternative node set definition.

Chapter 6

Discussion - Part II

6.1 Meshing Algorithms

While using a focused mesh geometry for fracture mechanics analysis is a widely implemented method, it does have alternatives. The non-focused mesh geometry can be created using a single global coordinate system where the circumferential element structure around the crack-tip for a focused mesh required the use of a local cylindrical coordinate system. As there is no need to use different coordinate systems, a single section - rather than the four sections in the focused mesh geometry (Figure 6-1(a)) - suffices to generate the top half of the mesh. Hence, there is no need to use linear multi-point constraints in the structure except to tie the top and bottom halves, as shown in Figure 6-1(b). Therefore, the non-focused mesh is easier to generate. The reason for initially selecting a focused mesh geometry was the expectation that it would provide more accurate results. Next, we will test this hypothesis by creating a non-focused mesh of same dimensions as in Table 4.1. In the vicinity of the crack front[1], the mesh density[2] of the focused mesh is preserved (Figure 6-2). Where the crack front in the focused mesh is surrounded by the user-defined number of

[1]Using the convention in Figure 4-2 (a) and Figure 6-1(b), the vicinity of the crack front is set to range from $X = 0$ to $X = 2a$, $Y = -a$ to $Y = a$ across the thickness, where a is the crack size.

[2]By meshing density we refer to the same number of elements and same biasing coefficient in the vicinity of the crack front (Table 4.2).

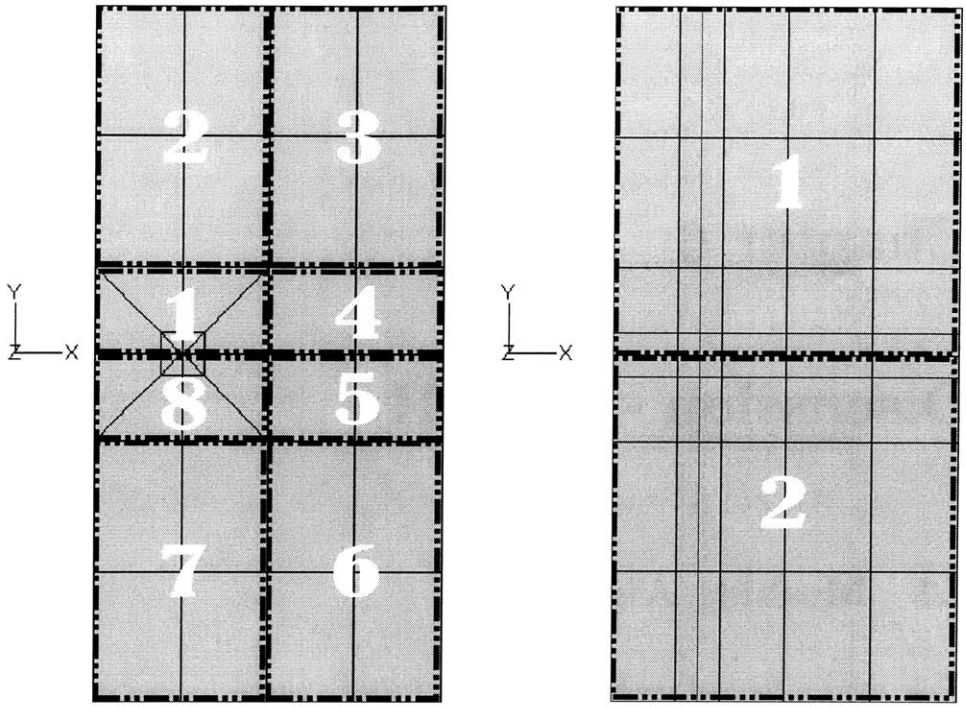

Figure 6-1: A 2-D schematic representation of the rectangular specimen for the (a) focused mesh (b) non-focused mesh created by MATLAB. Crack tip is located at $X = 1/4\,X_{max}$ and $Y = 0$. Numbers indicate sub-sections referred to in text.

circumferential elements, the crack front in the non-focused mesh is always surrounded by four elements at any given crack front location.

Figure 6-2 shows the non-focused mesh that was constructed. Figure 6-3 shows the vicinity of the crack tip for that mesh. The boundary conditions and loads were identical with the focused mesh as described in Chapter 4. The only difference in postprocessing is that instead of the first node away from the crack front, the displacements for the CFRD calculations were taken from the third node on the crack face away from the tip, which corresponds to the mid node of the second element. The ratio of that node' s distance from the crack front, r, to the crack length, a, is $r/a = 0.02$. Figure 6-4 shows the outcome of the simulation. We do observe the curious behavior of the edgeplane nodes across the crack front in the non-focused mesh as well. In all aspects, the calculations from the two meshing geometries seem to be equivalent. The next figure, Figure (6-5), compares the stress intensity factors

and directly calculated J-Integral values calculated from the two meshing algorithms for the same specimen[3] and plots the difference between the two. Compared to the focused mesh, the non-focused mesh calculates the mode I values to be 1% higher along the crack front. The difference in mode II calculations have a varying value of up to 0.2% on the midplane nodes, and up to 1% on the edgeplane nodes. The difference in mode III is only significant at the crack front ends, and reaches a value of 4%. The J-Integral calculations were compared using the direct domain integration method, and J's from the non-focused mesh are 2% higher than the focused mesh readings. As the difference between the two meshing algorithms amounts to only 1% on the reliable midplane node readings, we adopt the non-focused mesh geometry for further simulations, because of its ease of creation.

6.2 Midplane vs. Edgeplane Nodes

We have observed earlier that the stress intensity factors calculated at the edgeplane nodes across the crack front are contour-dependent. In this section, we try to formulate the contour dependency. It is worth noting that it is the area covered by each contour that is the variable, not the contour number. Yet, the contour numbers increase with increasing area and provide a qualitative frame for analysis.

We have also noticed that the stress intensity factors plotted along the crack front resemble a sinusoidal function as shown in Table 6.1, where $u = 2\pi(Z/Z_{max})$. For the midplane nodes, this shape function is contour-independent, while the amplitude of the function constructed using the edgeplane nodes is contour-dependent. Using the curve fitting toolbox in MATLAB, we construct three best-fit curves for each stress intensity factor, one from the midplane nodes, one from the edgeplane nodes, and the last one from all nodes for each contour. The spikes for K_{III} the readings at $Z = 0$ and $Z = Z_{max}$ are left out in all fit functions. We then plot the normalized[4] constants $K_I^{(base)}$, $K_I^{(amp)}$, $K_{II}^{(amp)}$, $K_{III}^{(amp)}$ against contours (Figures 6-6, 6-7, 6-8). The contour-

[3]Rectangular specimen under normal traction load; plane strain with $Amp/t = 1/20$.

[4]The stress intensity factors are normalized by the reference K_I solution.

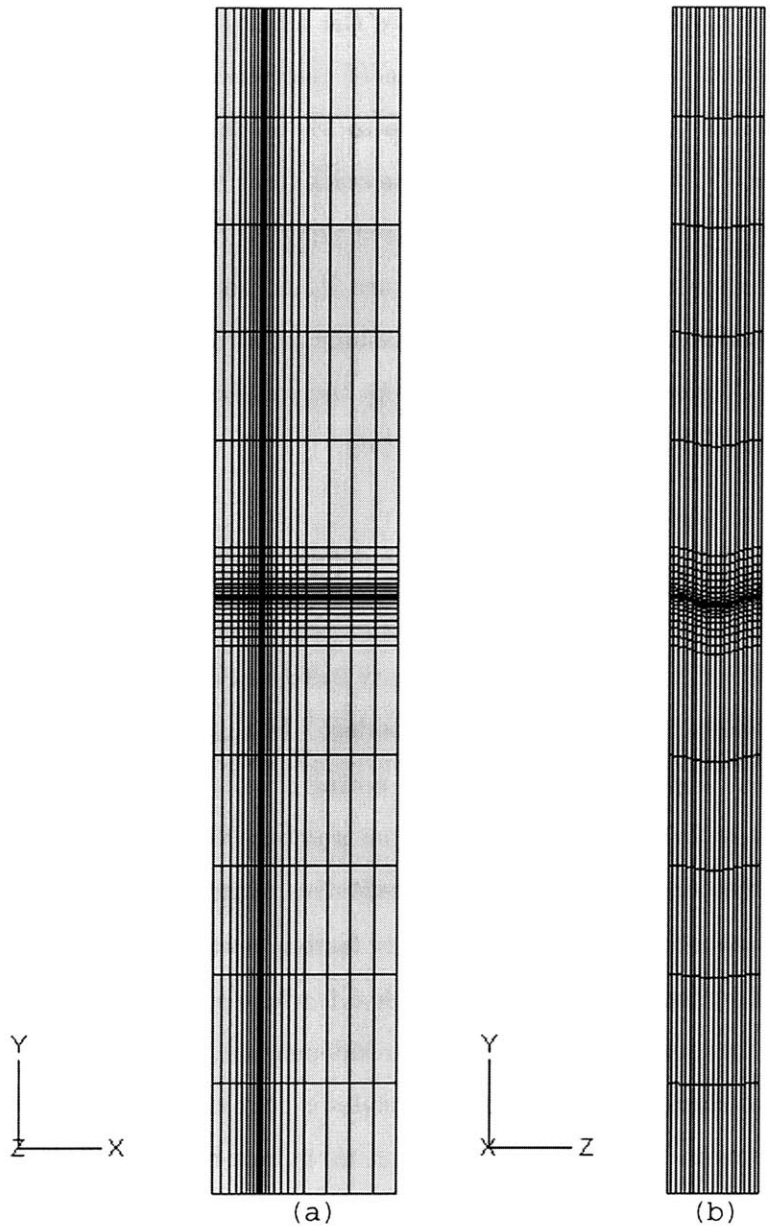

Figure 6-2: Non-focused mesh for the rectangular specimen tested under normal traction.

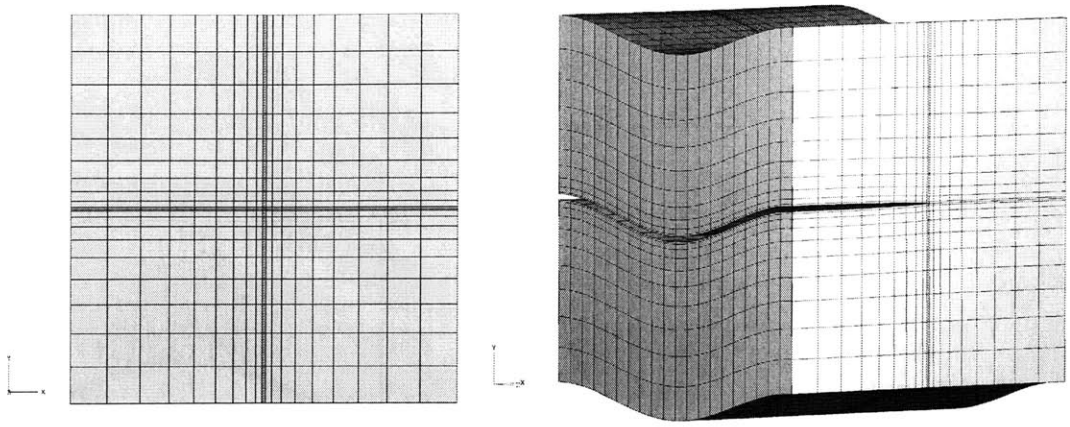

Figure 6-3: Views of the mesh geometry in the vicinity of the crack front for the non-focused mesh.

Mode I	$K_I = K_I^{(base)} + K_I^{(amp)} \cos(2u + \varphi)$
Mode II	$K_{II} = K_{II}^{(amp)} \cos(u + \varphi)$
Mode III	$K_{III} = K_{III}^{(amp)} \sin(u + \varphi)$

Table 6.1: Form of the best fit function to approximate the behavior of the stress intensity factors along the out-of-plane sinusoidal crack front.

independent numerical values for the above mentioned constants are summarized in Table 6.2 and compared to the results obtained from the CFRD method. Both the midplane and edgeplane best-fit curves presented here have a fit of $R^2 \geq 0.90$.

In all models, the first contour is left out of the discussion, as it is widely acknowledged that the first contour around the crack tip in a non-focused mesh does not provide accurate results.

The amplitude for the best fit curve by the midplane nodes provide a constant value for the parameters describing K_I, while the edgeplane nodes seem to be providing a diminishing best fit amplitude up to contour 5. Farther away from the crack front, the best fit amplitude provided by the edgeplane nodes seems to be approaching the constant value obtained from the midplane nodes. A similar observation can be made for base value. The midplane nodes for the parameter describing mode II

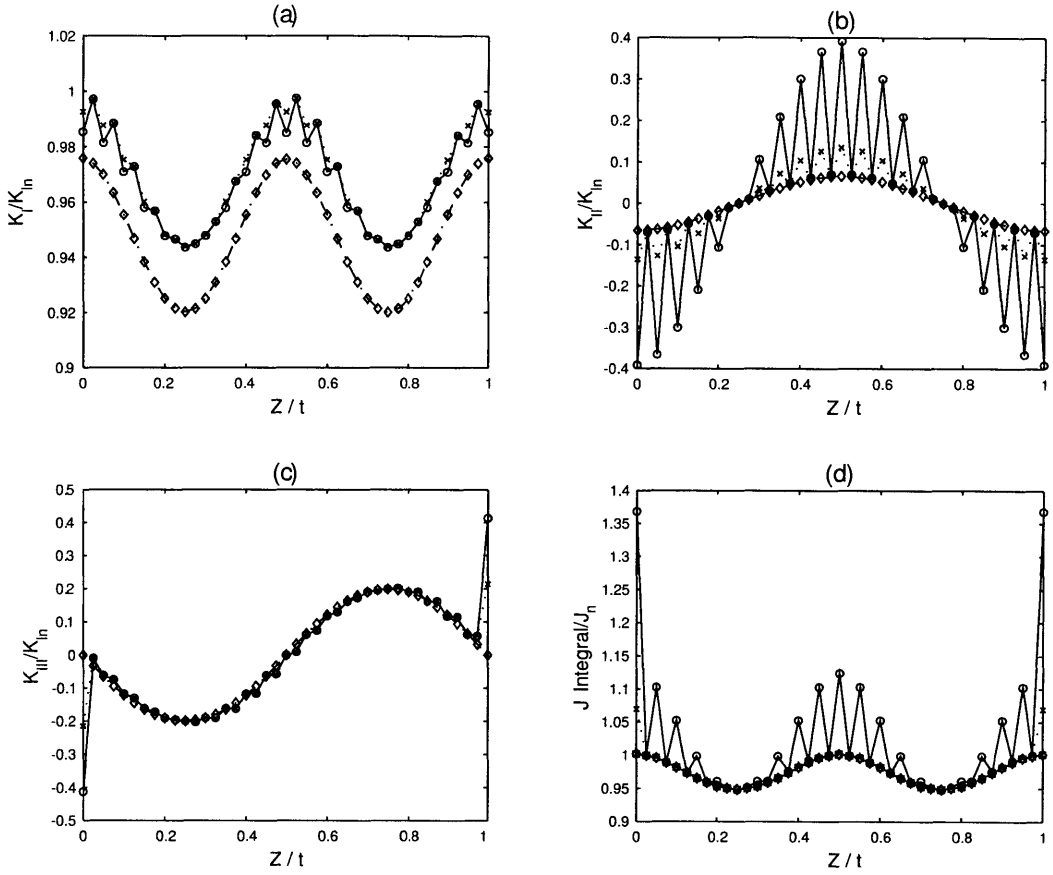

	(a),(b),(c)	(d)
legend	× Contour4 ○ Contour8 ◇ CFRD	× Contour4 (II) ◇ Contour4 (DI) ○ Contour8 (II) □ Contour8 (DI)
normalized by	$K_{I_n} = \sigma\sqrt{\pi a}\,F(a/b)$ $F(a/b) = \frac{1-0.5(a/b)+0.370(a/b)^2-0.044(a/b)^3}{\sqrt{1-(a/b)}}$	$J_n = \frac{K_{I_n}^2}{E/(1-\nu^2)}$

Figure 6-4: Superimposed and normalized (a) K_I (b) K_{II} (c) K_{III} and (d) J-Integral readings for the rectangular specimen using the non-focused mesh ($Amp/t = 1/20$, plane strain).

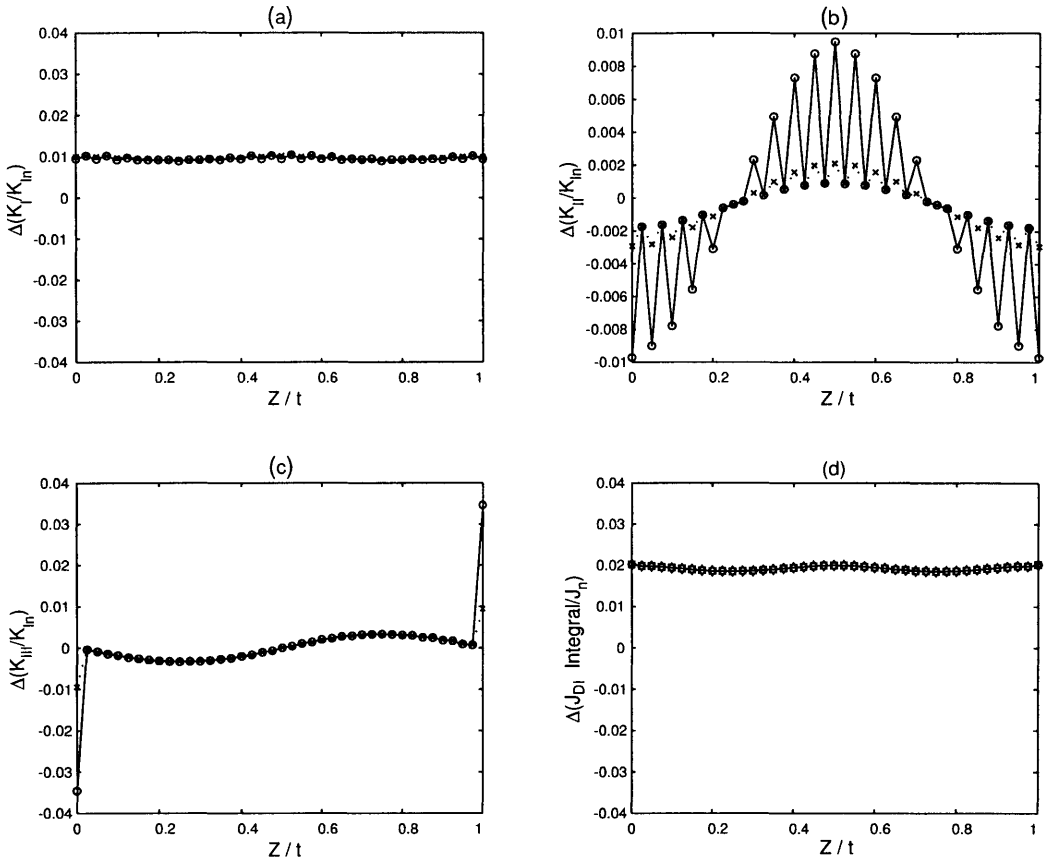

	(a),(b),(c)	(d)
legend	× Contour4 ○ Contour8 ◇ CFRD	× Contour4 (II) ◇ Contour4 (DI) ○ Contour8 (II) □ Contour8 (DI)
normalized by	$K_{I_n} = \sigma\sqrt{\pi a}\ F(a/b)$ $F(a/b) = \frac{1-0.5(a/b)+0.370(a/b)^2-0.044(a/b)^3}{\sqrt{1-(a/b)}}$	$J_n = \frac{K_{I_n}^2}{E/(1-\nu^2)}$

Figure 6-5: The difference in calculated stress intensity factors and J values for the non-focused mesh and the focused mesh (NF-F) for the rectangular plane strain specimen with a stress load ($Amp/t = 1/20$).

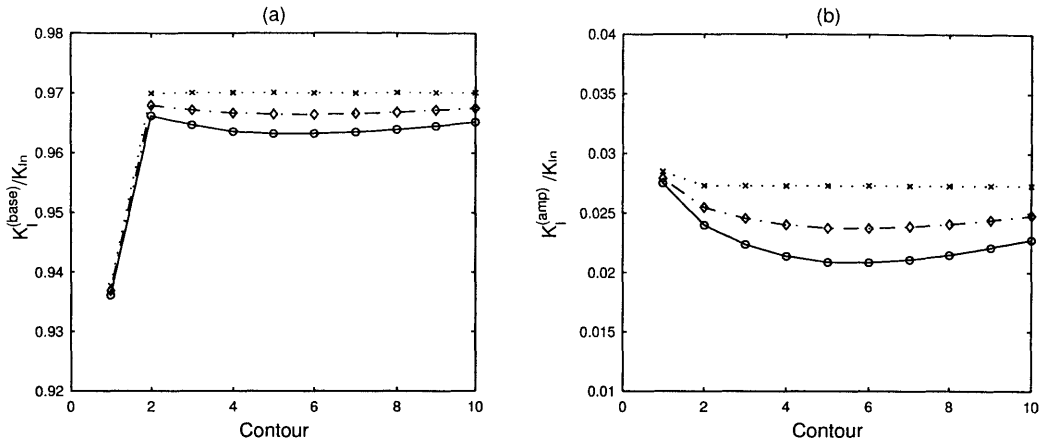

Best Fit	function	$K_I = K_I^{(base)} + K_I^{(amp)} \cos(2u + \varphi)$
	obtained from	× Midplane Nodes ○ Edgeplane Nodes ◇ All Nodes

Figure 6-6: Best fit plots for (a) base and (b) oscillatory parts of mode I stress intensity factors for specimen under normal traction load, where $K_I = K_I^{(base)} + K_I^{(amp)}$ (Plane Strain, $Amp/t = 1/20$).

	Numerical Analysis			CFRD		
	Base value $K_\alpha^{(base)}/K_{I_n}$	Amplitude $K_\alpha^{(amp)}/K_{I_n}$	Phase shift φ	Base value $K_\alpha^{(base)}/K_{I_n}$	Amplitude $K_\alpha^{(amp)}/K_{I_n}$	Phase shift φ
$\alpha = I$	0.9701	0.0273	0	0.9474	0.0277	0
$\alpha = II$	0	0.0688	π	0	0.0613	π
$\alpha = III$	0	0.2009	π	0	0.1939	π

Table 6.2: Constants for the best fit function to approximate the behavior of the stress intensity factors along the out-of-plane sinusoidal crack front for the specimen under far normal traction load. (Plane Strain, $Amp/t = 1/20$).

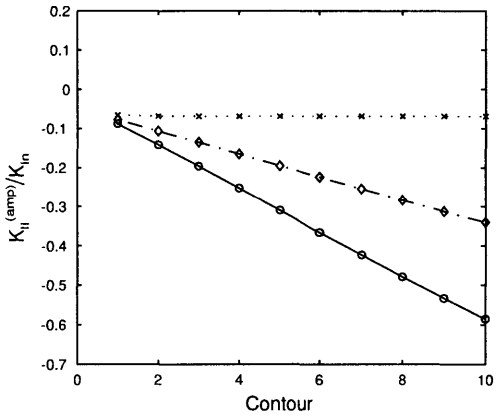

Best Fit	function	$K_{II} = K_{II}^{(amp)} \cos(u + \varphi)$
	obtained from	× Midplane Nodes ○ Edgeplane Nodes ◇ All Nodes

Figure 6-7: Best fit plots for mode II stress intensity factors for specimen under normal traction load (Plane Strain, $Amp/t = 1/20$).

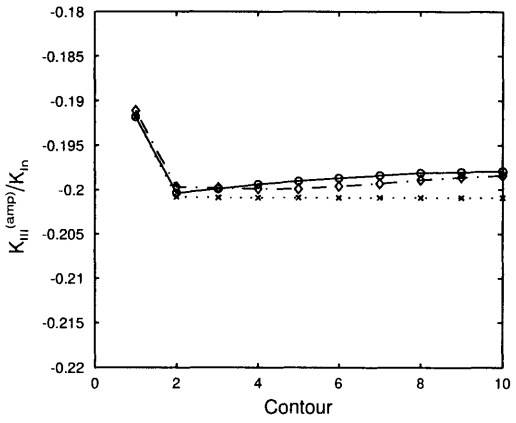

Best Fit	function	$K_{III} = K_{III}^{(amp)} \sin(u + \varphi)$
	obtained from	× Midplane Nodes
		○ Edgeplane Nodes
		◇ All Nodes

Figure 6-8: Best fit plots for mode III stress intensity factors for specimen under normal traction load (Plane Strain, $Amp/t = 1/20$).

follow a constant value, while the magnitude of the best fit amplitude provided by the edgeplane nodes seems to be increasing without bounds. In the case of mode III, the midplane nodes do provide a constant value as we move away from the crack tip. While the K_{III} values calculated from the edgeplane nodes deviate from the mid plane readings, the difference between the two readings seems to be becoming constant at around 1% as we move away from the crack tip.

It is worth reminding at this point that the foregoing stress and displacement fields for the three modes of loading represent the asymptotic fields as $r \rightarrow 0$ may be viewed as the leading terms in the expansions (Equation 1.6) of these fields about the crack tip. The applied loading σ, the crack length a, specimen width b, and height h may affect the strength of these fields through the stress intensity factors. Therefore, we can express the stress intensity factor as $K = K(\sigma, a, b, h)$. As we move farther away from the crack front, boundary conditions of the specimen become dominant.

6.3 Far Field K_I-loading

Our next task is to isolate the remote K-field from the effects of other boundary conditions. This can be achieved by applying a far field K-load to a region. As noted in Chapter 3, we can calculate the stress intensity factors from crack face displacements for any load at the specimen boundaries. It is possible to reverse this argument. To generate a pre-determined stress intensity factor, we can apply a displacement at the specimen faces on the $X - Z$ and $Y - Z$ planes. This process is referred to as 'applying a far field K-load'. We first place a local cylindrical coordinate system at the crack tip, to describe every point at the specimen boundary in terms of r and θ at any crack front location. We then set the magnitude of the desired mode I stress intensity factor and solve the corresponding CFRD equation to find the required r and θ displacement at each boundary node to reach that value. To avoid further normalization, we select $K_I^{\infty} = 1$. Normalization of the results by $K_{In} = 1$ has been explicitly expressed in the plots and $[K_I/K_{In}]$ represents units of the obtained values. The Z-coordinate of the local cylindrical coordinate system coincides with the global

Dimension	Value
$\frac{a}{b}$	$\frac{5}{12}$
$\frac{a}{t}$	10
$\frac{b}{h}$	$\frac{6}{5}$
$\frac{Amp}{t}$	$\frac{1}{10}$

Table 6.3: Dimensions of the specimen for the far field K_I load in relative terms.

Z-axis, and we apply displacement to all nodes at specimen boundaries by defining a displacement in the form of $D = D(r, \theta)$.

The relative specimen dimensions required to effectively apply far field K-load are given in Table 6.3. The Poisson's ratio was selected as $\nu = 0.3$. The characteristic element sizes for the innermost "tube" of elements around the crack front is $X = 1/100\,a$, $Y = 1/100\,a$, and $Z = 1/20\,Z_{max}$ where $a/Z_{max} = 10$. We verify the accuracy of our setup by applying a far field K_I-load. As expected, $K_I = 1$ with remaining stress intensity factors equal to zero (Figure 6-9). Next, we introduce surface roughness in terms of an out-of-plane sinusoidal function where $Amp/t = 1/10$ and calculate the mixed-modes stress intensity functions as explained in the previous section with the normal traction load.

Figures 6-10- 6-12 show the constants for the functions in Table 6.1 obtained from the simulations for the far field K_I-loading. The normalization process is not explicitly mentioned as we normalize by the magnitude of the applied mode I stress intensity factor, where $K_{In} = 1$. Similar to the normal traction load, the midplane nodes for the far field K_I-loading exhibit a contour-independent behavior where the stress intensity factors calculated at the edgeplane nodes are not constant. At the edgeplane nodes, they grow with increasing area, and unlike in the case of the normal traction load, the magnitudes $K_I^{(base)}$ and $K_I^{(amp)}$ at the edgeplane nodes keep growing at an increasing rate. The accuracy of our model can be confirmed by testing the

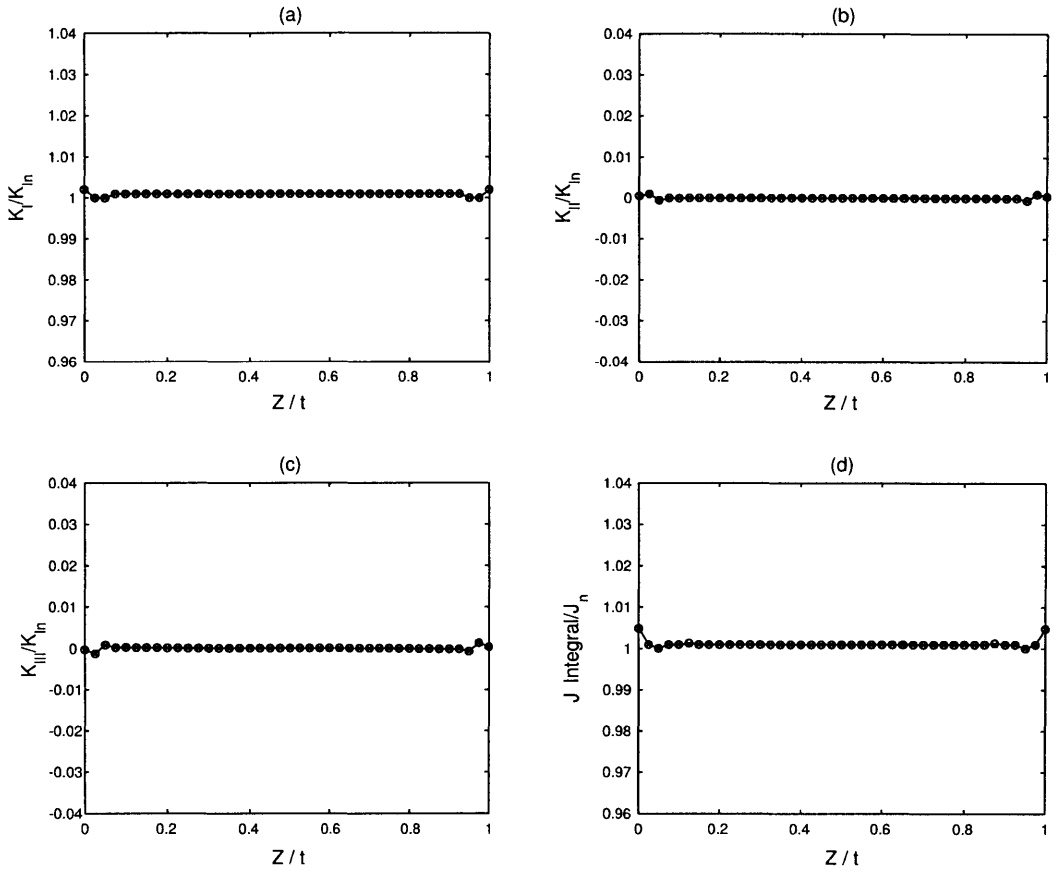

	(a),(b),(c)	(d)
legend	× Contour4 ○ Contour8	× Contour4 (II) ○ Contour8 (II)

Figure 6-9: Plots of (a) K_I (b) K_{II} (c) K_{III} and (d) J-Integral readings for the rectangular specimen using the non-focused mesh under far field "K_I-load" ($Amp = 0$, plane strain).

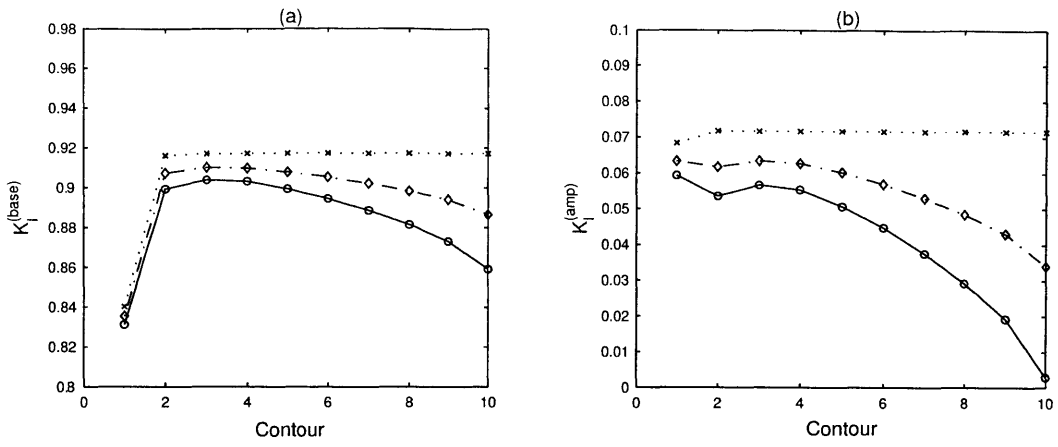

Best Fit	function	$K_I = K_I^{(base)} + K_I^{(amp)} \cos(2u + \varphi)$
	obtained from	× Midplane Nodes ○ Edgeplane Nodes ◇ All Nodes

Figure 6-10: Best fit plots for (a) base and (b) oscillatory parts of mode I stress intensity factors for specimen under far field K_I-load of unity, where $K_I = K_I^{(base)} + K_I^{(amp)}$ (Plane Strain, $Amp/t = 1/10$).

equality of the far field-local J-Integral to the thickness-arc length ratios. In other words, we would like to confirm,

$$J^{\infty} t = \int J_{local}(s)\, ds, \tag{6.1}$$

where s is the arc length along the sinusoidal crack front. For the tested specimen, where $Amp/t = 1/10$, arc length across the thickness is $S/t = 1.0924$. The far field J-Integral, J^{∞}, is calculated from the applied far field K_I- loading, while the local J-Integral values along the crack front, J_{local}, are calculated from Table 6.4. The equality holds, and we confirm the accuracy of our model. The constants in the best fit stress intensity factor functions obtained from the CFRD method are also presented in Table 6.4 and are in agreement with their numerical counterparts and serve to independently confirm the accuracy of the results.

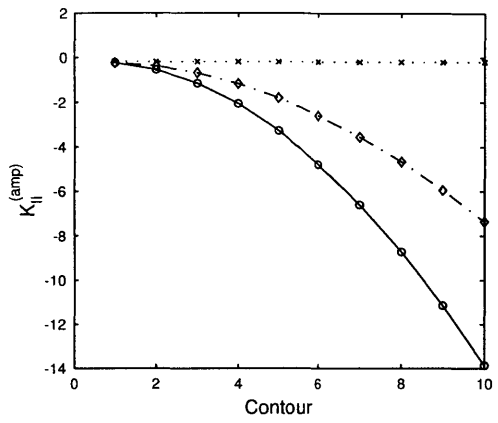

Best Fit	function	$K_{II} = K_{II}^{(amp)} \cos(u + \varphi)$
	obtained from	× Midplane Nodes o Edgeplane Nodes ◇ All Nodes

Figure 6-11: Best fit plots for mode II stress intensity factors for specimen under far field K_I-load of unity (Plane Strain, $Amp/t = 1/10$).

	Numerical Analysis			CFRD		
	Base value $K_\alpha^{(base)}/K_{I_n}$	Amplitude $K_\alpha^{(amp)}/K_{I_n}$	Phase shift φ	Base value $K_\alpha^{(base)}/K_{I_n}$	Amplitude $K_\alpha^{(amp)}/K_{I_n}$	Phase shift φ
$\alpha = I$	0.9173	0.0717	0	0.8906	0.0763	0
$\alpha = II$	0	0.1848	π	0	0.1463	π
$\alpha = III$	0	0.2924	π	0	0.3176	π

Table 6.4: Constants for the best fit function to approximate the behavior of the stress intensity factors along the out-of-plane sinusoidal crack front for the specimen under far field K_I- load of unity (Plane Strain, $Amp/t = 1/10$).

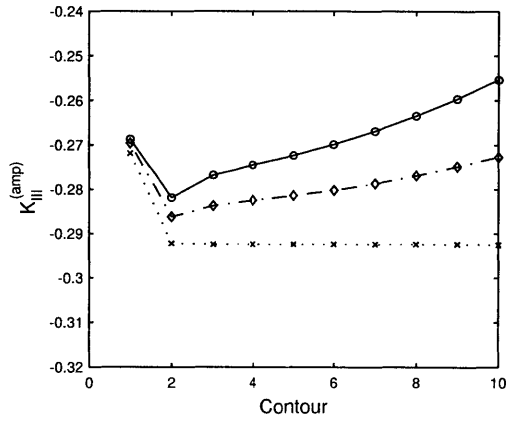

Best Fit	function	$K_{III} = K_{III}^{(amp)} \sin(u + \varphi)$
	obtained from	× Midplane Nodes
		○ Edgeplane Nodes
		◇ All Nodes

Figure 6-12: Best fit plots for mode III stress intensity factors for specimen under far field K_I-load of unity (Plane Strain, $Amp/t = 1/10$).

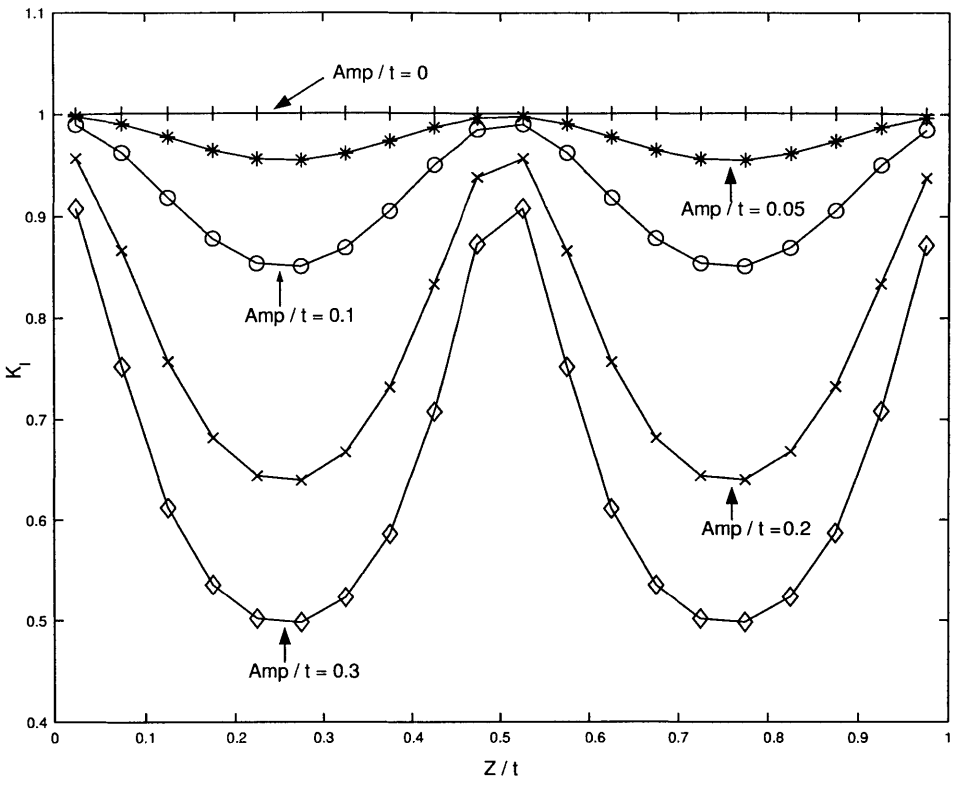

Figure 6-13: Varying Amp/t best fit plots for mode I stress intensity factors for specimen under far field K_I-load of unity (midplane nodes only).

6.4 Impact of Increasing Amplitude

So far, we used a single amplitude for the sinusoidal crack surface to solve for the stress intensity factors under far field K_I-loading. We would like to change the sinusoidal crack surface amplitude relative to the specimen thickness (Amp/t), and observe the change in the constants that shape the best fit function given in Table 6.4. As Amp/t increases, we observe that the stress intensity factors do not follow the form suggested in the previous sections.

Figure 6-13 plots normalized[5] K_I values obtained from the reliable midplane nodes against thickness for increasing Amp/t. Even though both the maxima and minima

[5]The specimen is loaded by a far field K_I of unity.

of the best fit curve drop with increasing Amp/t, the drop in the minima is larger. In loose terms, we can say that the minima "sags" mode than the maxima, suggesting a solution in the form of a cosine series. Hence, by generalizing the expressions obtained before (Table 6.1), we can express the stress intensity best fit functions as

$$K_I = \sum_{\lambda=0}^{\infty} \left[K_I^{(\lambda)} \cos\left(\lambda u + \varphi\right) \right], \tag{6.2}$$

$$K_{II} = \sum_{\lambda=0}^{\infty} \left[K_{II}^{(\lambda)} \cos\left((2\lambda+1)\, u + \varphi\right) \right], \tag{6.3}$$

$$K_{III} = \sum_{\lambda=0}^{\infty} \left[K_{III}^{(\lambda)} \sin\left((2\lambda+1)\, u + \varphi\right) \right]. \tag{6.4}$$

For our calculations, we will only use the first few terms of the series, namely, $\lambda = 0, 1, 2$ for K_I and $\lambda = 0, 1$ for K_{II} and K_{III}. The desired output is the stress intensity factors plotted against increasing Amp/t. Figures (6-14) - (6-16) show the constants K_α^λ that describe the stress intensity factors along the crack front for a specimen under far field K_I-loading.

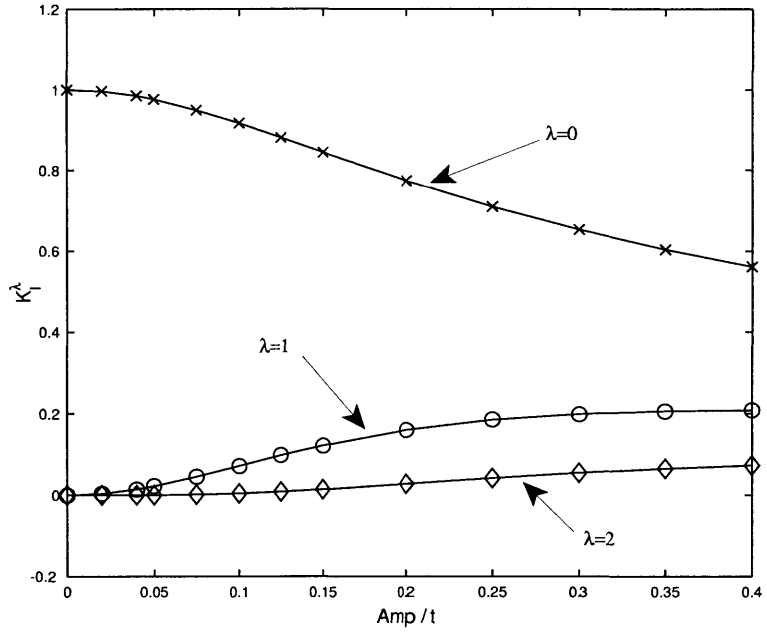

Figure 6-14: Plot of constants K_I^{λ} for various Amp/t for specimen under far field K_I load of unity.

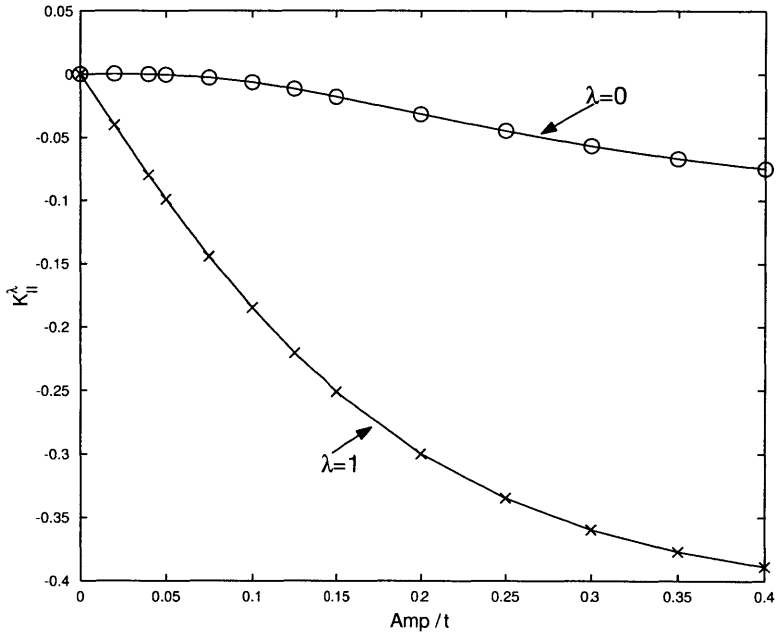

Figure 6-15: Plot of constants K_{II}^{λ} for various Amp/t for specimen under far field K_I load of unity.

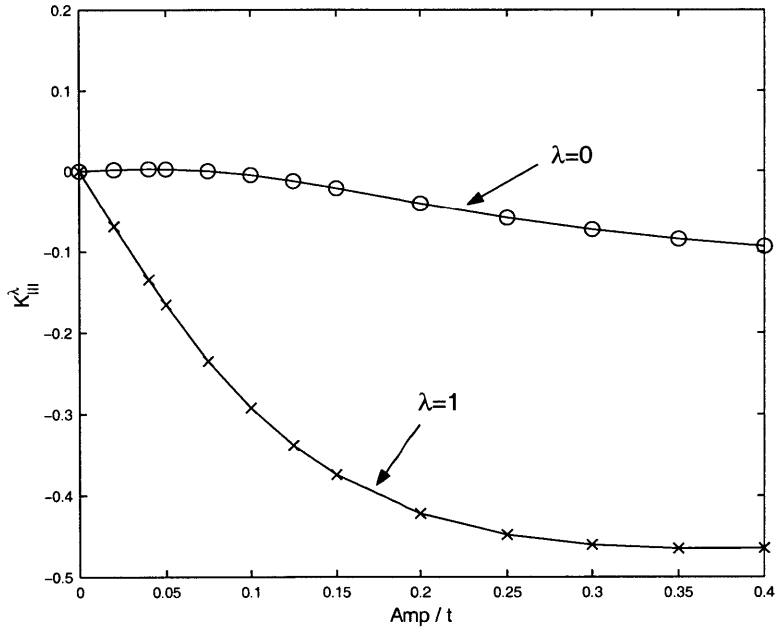

Figure 6-16: Plot of constants K^{λ}_{III} for various Amp/t for specimen under far field K_I load of unity.

Chapter 7

Conclusions and Future Work

Three-dimensional mixed-mode LEFM analysis using domain interaction integrals was presented in this work. First, the crack geometry to result in a mixed-mode analysis was created and the methodology for analysis was laid out. The model was then analyzed in ABAQUS, a commercially available package, to extract K_I, K_{II}, K_{III} stress intensity factors, and the J-Integral. The results were then verified by the Crack Front Relative Displacement (CFRD) method to verify the accuracy of the stress intensity factors, and the J-Integral obtained from the interaction integrals was compared to the directly-calculated J-Integrals. The parameters calculated from the edgeplane nodes in the interaction integrals exhibit a contour-dependent behavior providing inaccurate values. This could be tied to the definition of the auxiliary stress and strain fields. The assumption of zero divergence might not hold in the case of an oscillatory basis vector moving along the crack front - similar to the case simulated in this study. As the ABAQUS documentation does not provide details on its assumptions and definition of the auxiliary fields, the source of this error remains unresolved.

The purpose of this study is to establish a relationship between the three dimensional mixed-mode stress intensity factors and crack surface roughness. The surface roughness is modelled as the ratio of a sinusoidal crack amplitude to specimen thickness, Amp/t. Applying a far field K load to the specimen and using the reliable stress intensity factors calculated from the midplane nodes in ABAQUS, we formulate the

mode I, II, and III stress intensity factors as a function of the applied far field K_I load in the form of a cosine function.

The model used to establish the K-functions only utilizes the numerical results at the midplane nodes due to the inaccurate values at the edgeplane nodes. Therefore, the source of error in the software package that results in inaccurate stress intensity factors at the edgeplane nodes needs to be investigated. Moreover, the K-functions should also be tested for various Poisson's ratios.

Appendix A

MATLAB Codes

This Appendix summarizes the algorithm behind the MATLAB codes used in performing the analysis. Programs are classified as pre- and postprocessing codes. The first section discusses preprocessing for different setups, while the second section is focused on postprocessing codes.

A.1 Preprocessing Codes

Preprocessing includes mesh generation as well as the creation of the input file that will be processed in ABAQUS. The idea behind preprocessing was to create a flexible finite element input file that could accommodate changes in geometry, number of elements in the model, and material properties. The output of that code is a single and complete .inp file, ready to be processed in ABAQUS.

The code uses 27-node hexahedral elements in the analysis and is written for isotropic linear elastic fracture mechanics analysis. All preprocessing codes give the user the same flexibility to determine the dimensions, material properties, magnitude of load to be applied, and the number of elements to be assigned to each section of the model. The mesh was divided into real (focused mesh) or virtual (non-focused mesh) sections where the user could define the density of the mesh by assigning a pre-determined number of elements for that section and employing node-biasing near crack tip. The first layer of elements surrounding the crack tip are quarter-point

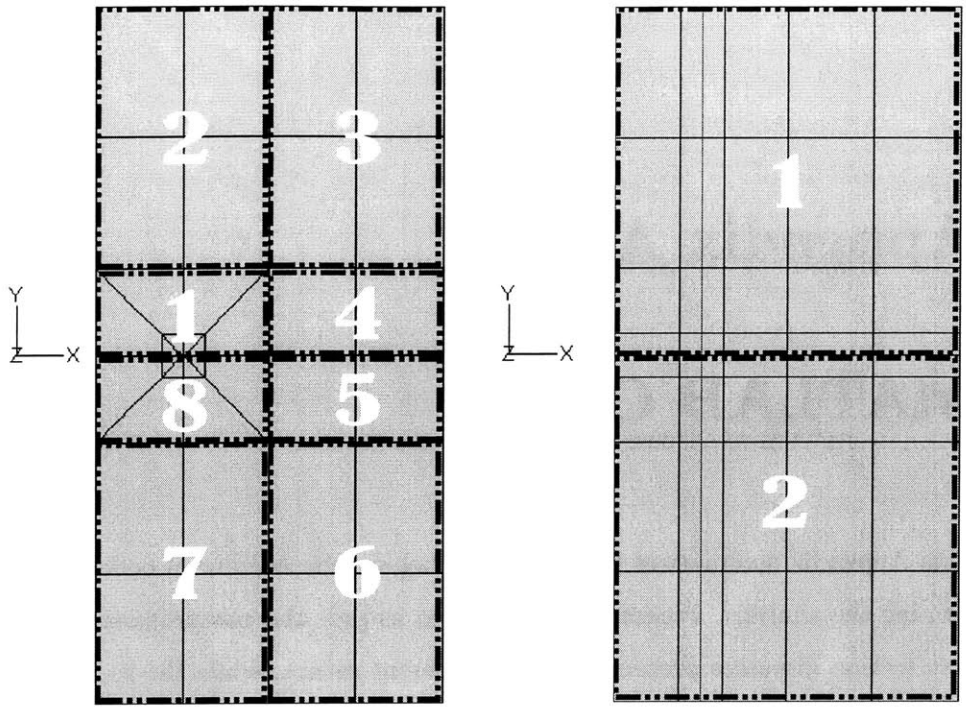

Figure A-1: A 2-D schematic representation of the rectangular specimen for the (a) focused mesh (b) non-focused mesh created by MATLAB. Crack tip is located at $X = 1/4\,X_{max}$ and $Y = 0$. Numbers indicate sub-sections referred to in text.

elements.

ABAQUS was asked to calculate the J-Integral values both using interaction integrals through K's and directly using the domain integral method. In cases where the local virtual crack propagation direction changes due to changes in specimen geometry, the crack propagation directions used for the crack front node sets were automatically updated.

A.1.1 Focused Mesh

Four unique meshes that constituted the top half of each geometry were tied to each other by defining linear multi-point constraints using built-in functionality in

ABAQUS[1]. The bottom half was then generated using the built-in mirroring functionality in ABAQUS [20].A global cartesian coordinate system with origin at the lower left hand corner of the top half has been set.

The first section is adjacent to the crack and is focused on to the crack tip, located at $X = 1/4\,X_{max}$ and $Y = 0$ in (Figure A-1(a)). This section has the shape of a rectangle with its X-dimension twice the size of its Y-dimension. As this piece will be duplicated by mirror imaging on the $X - Z$-plane, the final geometry around the crack tip is planned to be a square in the $X - Y$-plane. Hence, when the user defines the crack size, he defines the Y-dimension of this section, which is equal to the crack size, as well as the X-dimension, which equals twice the crack size. The schematic representation (Figure A-1(a)) is modelled using parametric input values $r_{el} = 2$ and $\theta_{el} = 4$. This section was created using circumferential elements around the crack tip. Introducing local cylindrical coordinates at the crack tip, nodes were placed around the tip. Node distances from the tip were determined by the number of elements within the section in each direction, dimensions of the crack, and by the biasing factor. In a sense, the crack tip is wrapped with a user-defined number of elements (θ_{el}-elements) and a user-defined number of layers (r_{el}-elements). While the r_{el}-elements are biased towards the crack tip, the θ_{el}-elements are homogenously distributed around it. All nodes in a given ring about the tip have either the same vertical or horizontal distance from the crack tip; hence they have the shape of an inverse " U " rather than a semi-circle (Figure 4-4). The number of θ elements has to be a multiple of four, as the " U " shape is divided in four equal sections, to make each circumferential element of the same size.

The height of the specimen and the user defined number of elements required to fill this space are the only new variables needed to create the second section of the mesh. The local coordinate system coincides with the global cartesian coordinate system. The height, less the crack length (which equals the height contribution from the first section) is the desired dimension of the second section in the Y-direction.

[1]A discussion of the multi-point constraints can be found in the ABAQUS manual [20], Section 20.

The X-dimension of the section, like the first section, is twice the size of the crack length. Moreover, the number of elements in the X-direction for the second section is also fixed, equaling the number of neighboring elements of Section 1, i.e., half of user-defined θ_{el}-elements. Once the dimensions and number of elements to fill these dimensions are determined, the nodes in Section 2 are generated through equal spacing. Sections 2 and 4 are created in a similar way. The third requires two additional user-defined input variables, namely, b, the total length of the specimen in the X-direction, and the number of elements to be used in that direction. All the variables to generate the fourth section are already defined at this point, and this section is generated as discussed above. Once a two-dimensional model is complete, additional nodes are extruded in the third direction. For the rectangular specimens, this extrusion is in the global Z-direction. When a thick cylinder with a penny shaped crack is modelled, a local cylindrical coordinate system is introduced where the Y-coordinate of the global cartesian coordinate system coincides with the z-coordinate of the local cylindrical coordinate system. The model is then extruded in the global θ-direction.

Even though the nodes have been generated, the elements have not been created yet. Element definition is described in detail in the ABAQUS manual, Section 2.2.1 [20]. For the models considered, 27-nodes characterize an element, and the required node ordering is given in Section 14.1.4 of the ABAQUS manual [20]. The numbering of these 27-nodes change as the user changes the number of elements in the model. To overcome this problem, a dynamic numbering scheme that automatically updates the node numbering during element creation has been coded. The remaining elements in the section were created incrementally from the master element that was just created[2]. The elements for the remaining three sections were created in a similar fashion.

Once all the elements for the top half of the specimen are generated, the MATLAB code creates the nodes for the bottom half by mirroring all node coordinates on the global $X - Z$-plane and assigning them node numbers. The elements for the bottom

[2]Incremental element generation is discussed in ABAQUS manual, Section 2.2.1 [20]

half of the model are created using the built-in ABAQUS functionality to generate elements by defining the $X-Z$ plane as the mirror plane. For element generation by mirroring, the code calculated the required input parameters, namely the number of elements and nodes in the top half of the model that has already been created.

Each of the eight sections constituting the model has a total of six faces in three dimensions. Node numbers for nodes located on these faces are captured in 48 node sets. The resulting node sets were later used either to apply linear multi-point constraints (i.e., to tie sections) or boundary conditions. The crack was simulated by not applying multi-point constraints for the left half of the first section, namely, for X-values smaller than the crack length, while $Y = 0$ on the global coordinate system. Node numbers at the free crack faces were stored as well. During postprocessing the displacements of the crack face nodes were used to calculate the stress intensity factors through Crack Face Relative Displacement (CFRD).

Once the node numbers for nodes on the crack faces are captured, the node coordinates in the global Y-direction are modified to incorporate a sinusoidal out-of-plane crack, rather than the flat crack resulting from the element reflection. A cosine function of one full cycle and no phase shift is integrated in the geometry. To accomplish this modification, a local coordinate system is introduced where the user-defined amplitude of the crack face oscillation coincided with the maximum global Y-coordinate, and one full cycle of the cosine curve is mapped across the thickness in the global Z-coordinate. The new shape of the crack is extended through the global X-dimension. To apply load at the specimen ends perpendicular to the crack plane, the planes at $Y = Y_{max}$ and $Y = -Y_{max}$, are required to be flat surfaces. Therefore, the normal distance to the crack plane is also a variable in the cosines transformation function. The amplitude of the cosine function has its maximum, user-defined value at the crack face ($Y = 0$) and its minimum of zero at the ends where the load is applied ($Y = Y_{max}$ and $Y = -Y_{max}$) in the form presented in Equation (A.1):

$$Y = Y_0 + \left[Amp\left(1 - \frac{Y_0}{Y_{max}}\right)\right] \cos\left(2\pi \frac{Z_0}{Z_{max}}\right), \tag{A.1}$$

where Y_0 is the Y-coordinate of the node in the undistorted geometry, and Z_0 is the

point along the crack front.

Finally, all nodes are checked for their assigned degrees of freedom, as multiple boundary conditions for nodes eliminated through multi-point constraints are not allowed in an ABAQUS input file. Besides the .inp file, the preprocessing code also saves a .mat file. This MATLAB workspace file contains specimen dimensions, material properties and the original coordinates of the nodes at the crack faces that will be read and used during postprocessing.

While most of the code remains universal, a number of versions have been created to account for different shapes, boundary conditions and load characteristics. The rectangular specimen is tested for both plane strain and periodic boundary conditions under stress for various crack amplitudes. Each of the three load profiles, namely out-of-plane stress, shear traction, and far field constant K_I are applied to the rectangular specimen.

A.1.2 Non-focused Mesh

The focused mesh generator requires setting local coordinate systems to generate nodes for different sections. Moreover, checking nodes for multiple boundary conditions is computationally expensive for MATLAB. Moreover, linear multi-point constraint equations employed to tie sections are also expensive for ABAQUS.

In a focused mesh setup, elements around the crack tip are focused onto the tip. An alternative to a focused mesh geometry is the non-focused mesh (Figure A-1(b)). Unlike the focused mesh, where a large number of elements reside at the crack tip through the collapsed hexahedral element geometry, only four elements are neighboring the crack tip in the non-focused configuration, and at any position the crack tip consists of a single node. Unlike the large-sized node set that is dependent on the circumferential elements used in the focused mesh, the crack tip node sets for the non-focused mesh consist of just 2 nodes, one on each side of the mirror-imaged halves of the mesh. The non-focused mesh can be generated much quicker in MATLAB, and runs faster in ABAQUS. The small number of elements surrounding the crack tip has been considered a disadvantage of the non-focused mesh. That hypothesis is tested

for the purposes of this study.

A specimen modelled using a non-focused mesh geometry contains only two sections, top half and bottom half (Figure A-1(b)). Hence, the only linear multi-point constraint applied is to tie top and bottom halves. The user first defines the dimensions of the specimen, including the crack size. Again, a global cartesian coordinate system with the lower left hand corner of section 1 as the origin is set up. In the X-direction, starting from $x = 0$, MATLAB creates the nodes, biasing them onto the tip until the tip is reached. These node coordinates in the X-direction are then mirrored from the crack tip towards higher x-values. Once the crack tip is seeded from both sides totaling to a length twice the crack size, MATLAB linearly distributes nodes to the remaining section of the specimen in the x-direction. At this point, X-coordinates for all nodes in the model are set. The number of nodes to be distributed is calculated from the number of user-defined elements for both the biased as well as unbiased sections. Similar to the focused mesh, the mesh density near the crack tip contributes to the mesh characteristics in the Y-direction near the crack tip. The crack size is equal to the y-dimension to be seeded with a bias onto the crack tip using the same number of elements as in the biased section of the X-direction. The remaining variables to be determined are the number of elements to fill the non-biased sections in both X- and Y-directions. Unlike in separate sections of the focused mesh, the same node number incremental values are preserved throughout the model, since all node implementation is done using the global cartesian coordinate system. As a result, a single element definition and element generation script suffices to generate the elements for the entire model. Thus zoning is referred to as virtual sectioning.

Nodes located at the faces of both sections are captured in a node set, similar to the focused mesh. Unlike the focused mesh there is no need to tie sections - except for the top and bottom halves. Boundary conditions, load, and the crack are all modelled following the same guidelines as explained for the focused mesh (Section A.1.1). Finally, the crack is distorted to model a surface roughness the same way as in the focused mesh.

A.2 Postprocessing Codes

The purpose of the simulations is to inspect the variation of the mixed-mode stress intensity factors and J-Integral values across the thickness (or around the circumference) of the specimen for out-of-plane sinusoidal crack fronts. To that end, we need to examine the calculated K and J-Integral values as they vary through the thickness. Each setup is run twice, once to obtain the stress intensity factors (TYPE=K), and another time to obtain the J-Integral values (TYPE=J). The desired values are stored in the corresponding .dat files created during ABAQUS analysis. The postprocessing codes were written to read and analyze those files. In addition, postprocessing also incorporates an ABAQUS created report containing displacements for nodes located at crack faces, and the .mat file created by MATLAB during mesh generation.

Three files have been created for postprocessing purposes. The first one plots the normalized K_I, K_{II}, K_{III} and J-Integral values obtained from the interaction integral method, where the second file captures the J-Integral values calculated directly from the domain integrals. The last file calculates the stress intensity factors through the CFRD method (Chapter 3) by utilizing displacements of crack face nodes as the input. All values are normalized using the analytical solutions corresponding to the load and specimen shape (rectangular and cylindrical).

A.2.1 Analyzing ABAQUS Output

Within the code that analyzes the .dat files, a number of versions exist. The user needs to select the correct version depending on the geometry of the specimen and the applied load type. Three reasons can be cited for this differentiation. First, the user cannot apply shear traction or torsion directly, and needs to apply a displacement. After the analysis, effective shear traction or torsion values are compiled in an additional code included in codes written for that load type. Second, all readings are normalized using the analytical solutions by the dominant stress intensity factor expected to result from the load type. For example, if the specimen is sheared, all readings are normalized by the analytical K_{III} solution for the given geometry. The

analytical solution is built-in to the code and differs for each load type and specimen geometry. Third, desired values are plotted directly against the thickness for the rectangular specimen, but need to be transformed in the case of the cylindrical specimen.

When asked to calculate the stress intensity factors, ABAQUS creates a .dat file which includes the required K_I, K_{II}, and K_{III} values as well as the J-Integrals calculated from those values at each contour for every crack-front position node set across the specimen thickness or circumference. The postprocessing code reads that .dat file, captures the required values and stores them in a matrix where the columns correspond to the contours and the readings in the rows correspond to crack tips across the thickness or circumference. Four rows fully capture all the information at a crack tip in the following order: K_I, K_{II}, K_{III}, J. Every fifth row provides the reading for the same variable at the next crack tip across the thickness. The code also loads the MATLAB workspace file saved during pre-processing. This workspace file contains specimen dimensions and other useful information required for postprocessing, including material dimensions, load characteristics, and the number of elements used across the thickness.

If the specimen is under normal traction with a user-specified magnitude, the calculated stress intensity factors are easily normalized by the built-in analytical formula for mode I stress intensity factors using that magnitude and specimen dimensions. The normalized K_I, K_{II}, K_{III}, and J-Integral values for any crack amplitude at any contour can then be plotted against the thickness or circumference. If the load is shear traction or torsion, additional work is required. As shear traction or torsion cannot be applied directly to the specimen in ABAQUS, the user applies a displacement to the top and bottom surfaces. In the cartesian coordinate system, this corresponds to user defined node displacement at $Y = Y_{max}$ and $Y = -Y_{max}$ in the global Z- and $-Z$-directions. In the cylinder setup, torque can be applied by imposing a circumferential displacement in the local θ-direction at $Z = Z_{max}$ and $Z = -Z_{max}$. During post processing, the user is required to find the shear traction or torque resulting from the applied displacement. Shear traction can be extracted directly through

querying within ABAQUS Viewer by probing σ_{23} values at nodes where displacement was applied. This value can then be manually entered into the post processing file to calculate the built-in analytical solution for mode III stress intensity factor. To calculate the torque corresponding to circumferential displacement in the cylinder, the magnitude of the reaction forces at nodes where the displacement is applied are recorded in an ABAQUS report. The magnitude for each node is then multiplied with that node' s radial distance from the center of the cylinder to give the torque resulting from the displacement of that specific node. The sum of nodal torques give the torque applied to the cylinder. This number is then used in the built-in analytical solution to calculate the stress intensity factors for a thick cylinder with a penny shaped crack. Finally, the computational results are normalized by the analytical solution and plotted against θ. The J-Integral value is normalized by J calculated from the stress intensity factor corresponding to applied load characteristic [3].

A second code is written to read the .dat output file created as a result of direct J-Integral calculations (TYPE=J). Similar to the first code, MATLAB reads the .dat file and extracts the desired J-values, and places them in a matrix. While the columns of the matrix still represent contours around the crack, a single row captures the only available datum at a given crack tip across the thickness or circumference - the J-Integral values. Again the results are normalized by the J-Integral value calculated from the stress intensity factor corresponding to load characteristics and plotted against crack tips for any given contour.

A.2.2 Stress Intensity Factors calculated from CFRD Method

The Crack Face Relative Displacement method is discussed in detail in Chapter 3. To use this portion of the postprocessing code, the user is required to create a report in ABAQUS consisting of displacements of nodes at crack faces. Nodes in question are collected in two node sets during preprocessing, one for the top crack face and another one for the bottom crack face. The field output report, created in ABAQUS under

[3]For example, if the applied load stress perpendicular to the crack plane, J is calculated using resulting K_I from the analytical solution

a unique nodal menu for the node sets at the top and bottom crack faces, contains spatial displacements $U1, U2$, and $U3$ based on the global coordinate system. Sorted by the ascending node labels, this report does not include column totals or column min/max. The report, as well as the .mat file created by this preprocessing code is read by the postprocessing file. The .mat workspace file contains the original coordinates of the nodes on the crack faces, material properties as well as specimen dimensions. The code reads the displacement of a node in all directions from the ABAQUS report and the corresponding original distance of that node from the crack tip from the workspace file. The displacements are then converted into the local coordinate system along the sinusoidal crack curve. The resulting crack openings are then plugged into the solutions obtained from CFRD calculations for each opening mode, normalized by the analytical solution for the setup, and plotted as a way to verify the accuracy of K' s obtained from the interaction integral method using ABAQUS. For the focused mesh, the nodes closest to the crack tip is used for the calculations while the third node set away from the crack tip is selected for the non-focused mesh. This choice is justified by the fact that the first ring of elements around the tip in a non-focused mesh provide inaccurate results.

Bibliography

[1] R.P. Reed. The economic effects of fracture in the united states. *U.S. Department of Commerce, National Bureau of Standards*, 647, 1983.

[2] A.A. Griffith. The phenomena of rupture and flow in solids. *Philosophical Transactions*, 1920.

[3] G.R. Irwin. Fracture dynamics. In *Fracturing of Metals*, pages 147–166, Cleveland, 1948. American Society for Metals.

[4] H.M. Westergaard. Bearing pressures and cracks. *Transactions of the American Society of Mechanical Engineers*, 61:A49–A53, 1939.

[5] G.R. Irwin. Analysis of stresses and strains near the end of a crack traversing a plate. *Journal of Applied Mechanics*, 24:361–364, 1957.

[6] C.F. Shih B. Moran. A general treatment of crack-tip contour integrals. *International Journal of Fracture*, 35:295–310, 1987.

[7] C.F. Shih B. Moran. Crack-tip and associated domain integrals from momentum and energy balance. *Engineering Fracture Mechanics*, 27:615–642, 1987.

[8] R.S. Dunham M. Stern, E.B. Becker. A contour integral computation of mixed-mode stress intensity factors. *International Journal of Fracture*, 12:359–368, 1976.

[9] B. Moran M. Gosz. An interaction energy integral method for computation of mixed-mode stress intensity factors along non-planar crack fronts in three dimensions. *Engineering Fracture Mechanics*, 69:299–319, 2002.

[10] J.R. Rice H. Gao. Shear stress intensity factors for a planar crack with slightly curved front. *Journal of Applied Mechanics*, 53:774–778, 1986.

[11] J.R. Rice. A path independent integral and the approximate analysis of strain concentration by notches and cracks. *Journal of Applied Mechanics*, 35:379–386, 1968.

[12] H. Rajaram. Three-dimensional fracture mechanics computations using tetrahedral finite elements. Master's thesis, Massachusetts Institute of Technology, 1999.

[13] J.R. Rice B. Budiansky. Conservation laws and energy release rates. *Journal of Applied Mechanics*, 40:201–203, 1973.

[14] F.Z. Li, C.F. Shih, and A. Needleman. A comparison of methods for calculating energy release rates. *Engineering Fracture Mechanics*, 21:405–421, 1985.

[15] D.M. Parks. A stiffness derivative finite element technique for determination of crack tip stress intensity factors. *International Journal of Fracture*, 10:487–502, 1974.

[16] J.D. Eshelby. *Energy relations and the energy-momentum tensor in continuum mechanics in inelastic behavior of solids.* McGraw Hill, 1970.

[17] R.J. Asaro D.M. Barnett. The fracture mechanics of slit-like cracks in anisotropic elastic media. *Journal of the Mechanics and Physics of Solids*, 20:353–366, 1972.

[18] W.S. Slaughter. *The Linearized Theory of Elasticity.* Birkhauser, 2002.

[19] C.H. Popelar M.F. Kanninen. *Advanced Fracture Mechanics.* Oxford University Press, 1985.

[20] *ABAQUS 6.3-1 Documentation.*

[21] G.R. Irwin H. Tada, P.C. Paris. *The Stress Analysis of Cracks Handbook, Third Edition.* McGraw Hill, 2000.

[22] M.C. Boyce M. Danielsson, D.M. Parks. Three-dimensional micromechanical modeling of voided polymeric materials. *Journal of the Mechanics and Physics of Solids*, 50:351–379, 2002.